Cell Reports

Article

Membrane damage by MBP-1 is mediated by pore formation and amplified by mtDNA

Graphical abstract

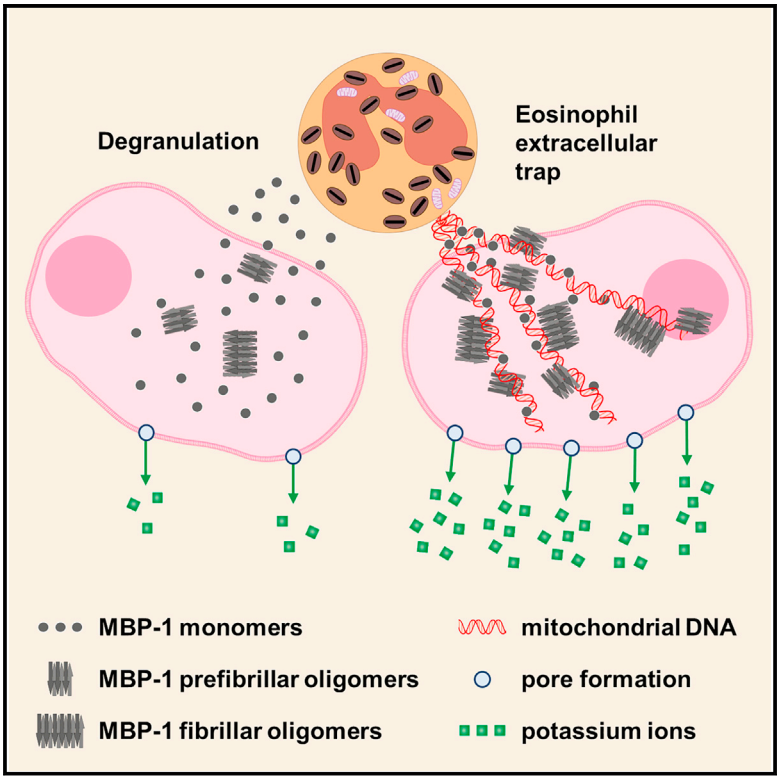

Authors

Lea Gigon, Philipp Müller, Beat Haenni, ..., Christoph von Ballmoos, Benoît Zuber, Hans-Uwe Simon

Correspondence

hans-uwe.simon@unibe.ch

In brief

MBP-1, a toxic granule protein in eosinophils, contributes to host defense and immunopathology. Gigon et al. demonstrate how MBP-1 forms small pores in lipid bilayers, causing membrane permeabilization and potassium leakage. Lack of CpG DNA methylation in bacterial and mitochondrial DNA within eosinophil extracellular traps amplifies the toxicity of MBP-1.

Highlights

- Mitochondrial DNA found in eosinophil extracellular traps amplifies MBP-1 toxicity
- Lack of DNA methylation in mitochondrial DNA is key for enhancing MBP-1 toxicity
- MBP-1 forms small pores, approximately 1 kDa in size, in lipid bilayers
- MBP-1 initiates plasma membrane permeabilization and efflux of potassium

Gigon et al., 2024, Cell Reports *43*, 114084
April 23, 2024
https://doi.org/10.1016/j.celrep.2024.114084

CellPress

Cell Reports

CellPress
OPEN ACCESS

Article

Membrane damage by MBP-1 is mediated by pore formation and amplified by mtDNA

Lea Gigon,[1] Philipp Müller,[2] Beat Haenni,[3] Ioan Iacovache,[3] Maruša Barbo,[1,4] Gordana Gosheva,[1,4] Shida Yousefi,[1] Alice Soragni,[5] Christoph von Ballmoos,[2] Benoît Zuber,[3] and Hans-Uwe Simon[1,6,7,*]

[1]Institute of Pharmacology, University of Bern, 3010 Bern, Switzerland
[2]Department of Chemistry, Biochemistry, and Pharmaceutical Sciences, University of Bern, 3012 Bern, Switzerland
[3]Institute of Anatomy, University of Bern, 3012 Bern, Switzerland
[4]Faculty of Pharmacy, University of Ljubljana, 1000 Ljubljana, Slovenia
[5]Department of Orthopedic Surgery, David Geffen School of Medicine, University of California, Los Angeles, Los Angeles, CA 90095, USA
[6]Institute of Biochemistry, Brandenburg Medical School, 16816 Neuruppin, Germany
[7]Lead contact
*Correspondence: hans-uwe.simon@unibe.ch
https://doi.org/10.1016/j.celrep.2024.114084

SUMMARY

Eosinophils play a crucial role in host defense while also contributing to immunopathology through the release of inflammatory mediators. Characterized by distinctive cytoplasmic granules, eosinophils securely store and rapidly release various proteins exhibiting high toxicity upon extracellular release. Among these, major basic protein 1 (MBP-1) emerges as an important mediator in eosinophil function against pathogens and in eosinophil-associated diseases. While MBP-1 targets both microorganisms and host cells, its precise mechanism remains elusive. We demonstrate that formation of small pores by MBP-1 in lipid bilayers induces membrane permeabilization and disrupts potassium balance. Additionally, we reveal that mitochondrial DNA (mtDNA) present in eosinophil extracellular traps (EETs) amplifies MBP-1 toxic effects, underscoring the pivotal role of mtDNA in EETs. Furthermore, we present evidence indicating that absence of CpG methylation in mtDNA contributes to the regulation of MBP-1-mediated toxicity. Taken together, our data suggest that the mtDNA scaffold within extracellular traps promotes MBP-1 toxicity.

INTRODUCTION

Eosinophils, together with neutrophils and basophils, belong to the granulocytes, a group of white blood cells (WBCs) derived in the bone marrow that is characterized by an abundance of cytoplasmic granules.[1] Historically, eosinophils were primarily seen as cytotoxic effector cells, responsible for defending against pathogens and participating in allergic and autoimmune reactions.[2] To combat invading pathogens, eosinophils undergo distinct processes, such as degranulation, respiratory burst, formation of eosinophil extracellular traps (EETs), and phagocytosis.[3] While the exact function of eosinophils remains debated, more recent findings have shown that they also possess properties related to immune regulation,[4–9] maintenance of tissue balance,[9–14] and facilitation of wound healing.[9,15–17]

Eosinophils store preformed inflammatory mediators in their cytoplasmic granules, allowing for fast release upon activation.[18] The cationic protein major basic protein 1 (MBP-1) plays a crucial role in both the regulatory and toxic roles of eosinophils.[19–21] In resting eosinophils, MBP-1 is encapsulated in a nanocrystalline structure within the core of the specific granules, ensuring its secure storage at high concentrations.[20] Upon eosinophil activation, MBP-1 is rapidly released from crystals and undergoes self-aggregation.[20] Previous research has demonstrated that MBP-1 specifically targets and disrupts the membranes of bacteria and parasites, leading to lysis and, ultimately, death of the pathogens.[20,22] On the other hand, dysregulation of MBP-1 release and function is associated with various diseases, such as asthma.[23] We have shown previously that the toxic effect of MBP-1 toward mammalian cells is attributed to its prefibrillar and fibrillar oligomers formed during the process of amyloid aggregation.[20] However, as these oligomers mature into fibrils, their toxicity is neutralized.[20] This process is similarly observed in extracellular MBP-1 deposits with limited tissue damage.[20] Such deposits have been reported under specific pathophysiological conditions triggered by intense eosinophil degranulation.[24–26]

In the extracellular space, MBP-1 is also detected in association with mitochondrial DNA (mtDNA) within the structure of EETs.[19] Activated neutrophils,[27] basophils,[28] and mast cells[29] have been shown to generate similar extracellular structures. These extracellular traps play a multifaceted role in the immune response, defending against various microbes by immobilizing and killing them to prevent their spread.[19,27,30] The associated antimicrobial mediators released from eosinophils and neutrophils are conveniently located adjacent to the extracellular DNA scaffold, which allows a more focused action of the toxic granule proteins and a reduction of tissue damage.[31,32] Such DNA-containing extracellular structures released from neutrophils, eosinophils,

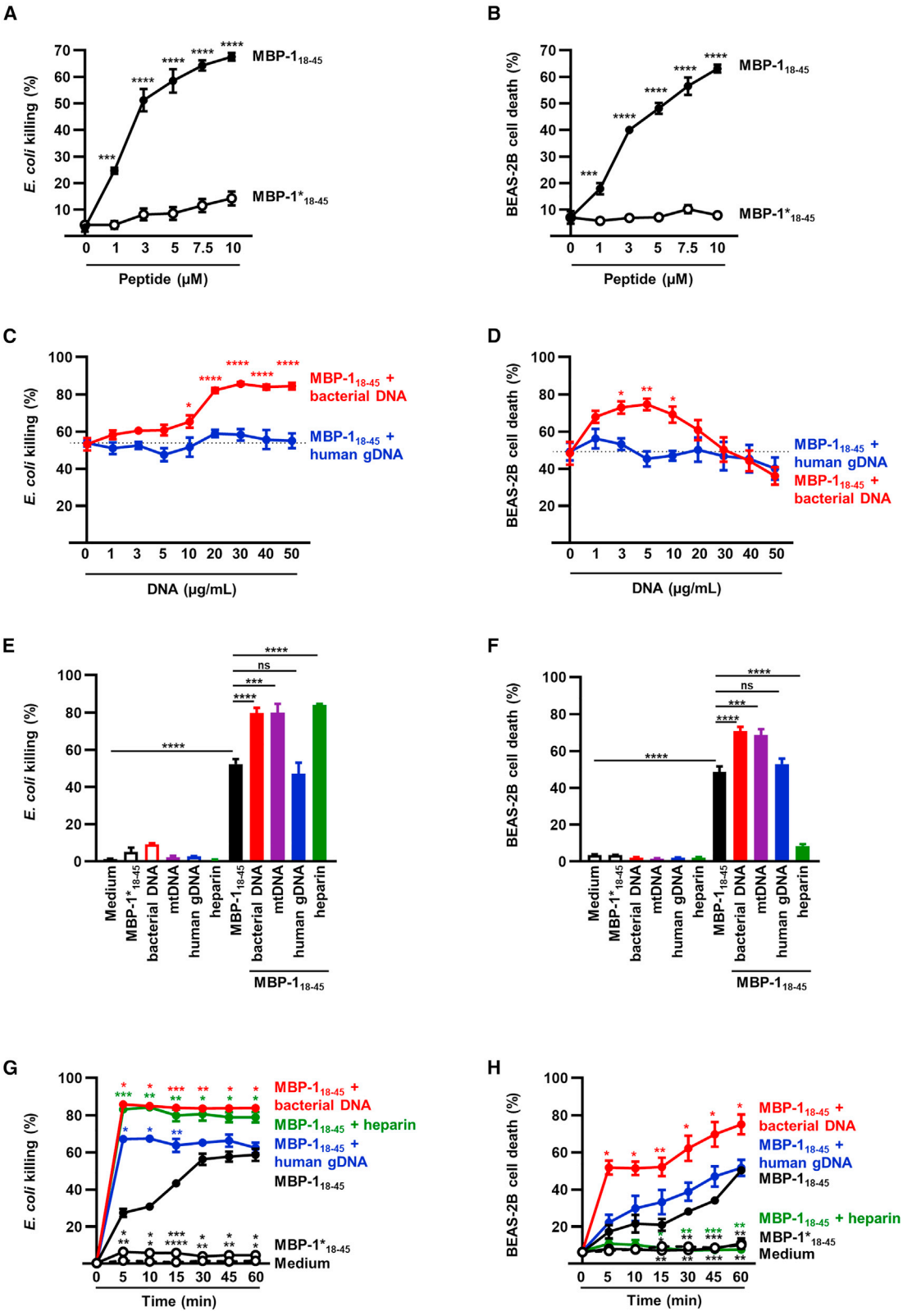

(legend on next page)

monocytes, and mast cells have been demonstrated in multiple infectious as well as allergic and autoimmune diseases,[33,34] highlighting the delicate balance required in their formation and resolution. The formation of EETs and neutrophil extracellular traps (NETs) has been shown to rely on reactive oxygen species (ROS) production but to be independent of autophagy.[35] Furthermore, glycolytic adenosine triphosphate (ATP) production and cytoskeletal rearrangement are required for the formation of NETs.[36] We have shown that the release of mtDNA is not linked to either cell death or shortening of eosinophils' or neutrophils' lifespan.[19,37] Whether eosinophil or neutrophil death occurs during extracellular trap formation and the source of the released DNA remain subjects of debate.[38] Some studies propose that extracellular traps consist of genomic DNA (gDNA) and that the release and extracellular trap formation occur upon cell death.[39,40]

In this study, our main objective is to elucidate the mechanism of MBP-1 toxicity toward microorganisms and mammalian cells and to investigate the role of extracellular dsDNA in regulating its antimicrobial activity. To achieve this, we utilized a specific peptide derived from MBP-1 (termed MBP-$1_{18–45}$) known to mimic the aggregation propensity and toxicity against bacteria and eukaryotic cells of the full-length protein.[20] We demonstrate an additional function of mtDNA within EETs, amplifying MBP-1's toxicity. Additionally, our findings contribute further evidence toward elucidating the origin and mechanism of extracellular DNA in EETs. Our results reveal that the absence of CpG DNA methylation plays a crucial role in the regulation of MBP-1's toxicity, leading to increased and accelerated activity in the presence of mtDNA and bacterial DNA but not human gDNA. Furthermore, heparin, while alleviating MBP-1-mediated damage to mammalian cells, enhances its antibacterial effects, offering promise for therapeutic applications. Last, our data imply that MBP-1 induces rapid cell death in human bronchial epithelial cells by causing plasma membrane damage through the formation of small pores with a resulting imbalance of ion homeostasis.

RESULTS

mtDNA-mediated enhancement of MBP-1 toxicity on bacteria and human bronchial epithelial cells

MBP-1 is well known for its strong antibacterial characteristics.[22] Conversely, its interaction with mammalian cells can lead to host toxic effects, particularly in eosinophil-related diseases.[20,41] To evaluate the efficacy of MBP-1_{18-45}, we tested its bactericidal activity against *Escherichia coli* (*E. coli*) (Figure 1A) as well as its cytotoxic potential on human bronchial epithelial alveolar cells (BEAS-2B) (Figure 1B). We used GFP-expressing *E. coli*, quantified the reduction in GFP levels as an indicator of bacterial killing (Figure 1A), and determined the viability of BEAS-2B cells based on the uptake of propidium iodide (PI) (Figure 1B) upon exposure to 1–10 μM MBP-$1_{18–45}$. Incubation of both *E. coli* and BEAS-2B cells with MBP-$1_{18–45}$ for 1 h resulted in a concentration-dependent reduction of viability (Figures 1A and 1B). We have demonstrated previously that the toxicity of MBP-1 depends on its ability to aggregate using a control peptide, termed MBP-$1^*_{18–45}$, that displayed diminished aggregation propensity, subsequently leading to a reduction in its toxic capabilities.[20] The control peptide was engineered through a three-point mutation, replacing three amino acids in critical aggregation-prone regions with proline. These mutations potentially impacted the peptide's ability to form secondary structures like β sheets or to engage in hydrogen bonding. They also altered its hydrophobicity profile and hindered the proper alignment needed for aggregation. In line with this, we showed no impact on the viability of *E. coli* and BEAS-2B cells after incubation with MBP-$1^*_{18–45}$ (Figures 1A and 1B), confirming the link between MBP-1 aggregation and its toxic functions. We opted for a peptide concentration of 5 μM in downstream experiments unless specified otherwise.

Recently, it has been reported that bacterial extracellular DNA contributes to the aggregation of amyloid proteins.[42] MBP-1 is also found in association with released mtDNA in EETs.[19] Mitochondria, including their mtDNA, generate similar danger signals within mammalian cells as bacterial DNA, likely due to their bacterial ancestry and relatively low levels of DNA methylation.[43] Therefore, we tested the effects of bacterial and human gDNA at various concentrations ranging from 1–50 μg/mL on MBP-$1_{18–45}$-mediated toxicity (Figures 1C and 1D). We observed that bacterial DNA significantly enhanced the toxicity of MBP-$1_{18–45}$ against *E. coli* (Figure 1C). Interestingly, lower concentrations of bacterial DNA (1–10 μg/mL) amplified MBP-$1_{18–45}$-mediated cell death of BEAS-2B cells, whereas higher concentrations led to unaffected or even reduced toxicity (Figure 1D). On the contrary, higher bacterial DNA concentrations (>20 μg/mL) induced even higher levels of bactericidal activity (Figure 1C), indicating a contrasting effect of distinct DNA concentrations

Figure 1. Toxicity toward microorganisms and mammalian cells mediated by MBP-$1_{18–45}$ in combination with different sources of DNA

(A and B) *E. coli*-GFP (A) and BEAS-2B cells (B) were treated with the indicated concentrations of MBP-$1_{18–45}$ (1–10 μM) for 1 h. MBP-$1^*_{18–45}$ was used as a negative control. Cell toxicity was assessed by the loss of GFP (A) or the uptake of PI (B) using flow cytometry. Data are representative of 3 independent biological replicates. The assays were performed in duplicates.

(C and D) *E. coli*-GFP (C) and BEAS-2B cells (D) were treated with MBP-$1_{18–45}$ in combination with the indicated concentrations of bacterial DNA or human gDNA (1–50 μg/mL) for 1 h. Cell toxicity was assessed by the loss of GFP (C) and the uptake of PI (D) using flow cytometry. Significances are shown against MBP-$1_{18–45}$ alone (dashed line). Data are representative of 4 independent biological replicates. The assays were performed in duplicates.

(E and F) *E. coli*-GFP (E) and BEAS-2B cells (F) were treated with MBP-$1_{18–45}$ in combination with bacterial DNA, mtDNA, and human gDNA for 1 h. Heparin and MBP-$1^*_{18–45}$ were used as negative controls. Cell toxicity was assessed by the loss of GFP (E) or the uptake of PI (F) using flow cytometry. Data are representative of 3 independent biological replicates. The assays were performed in duplicates.

(G and H) *E. coli*-GFP (G) and BEAS-2B cells (H) were treated with MBP-$1_{18–45}$ in combination with bacterial DNA and human gDNA for the indicated times. Heparin and MBP-$1^*_{18–45}$ were used as negative controls. Cell toxicity was assessed by the loss of GFP (G) or the uptake of PI (H) using flow cytometry. Significance is shown against MBP-$1_{18–45}$ alone (black). Data are representative of 4 independent biological replicates. The assays were performed in duplicates. All data are represented as mean ± SEM, and *p* values (ns, not significant; $^*p < 0.05$, $^{**}p < 0.01$, $^{***}p < 0.001$, $^{****}p < 0.0001$) were calculated using two-way ANOVA with Sidak's multiple comparisons (A–D) or Dunnett's multiple comparisons (G and H) and ordinary one-way ANOVA with Tukey's multiple comparisons (E and F).

on MBP-$1_{18–45}$-mediated toxicity in *E. coli* or BEAS-2B cells. Hence, we utilized DNA concentrations of 5 μg/mL for BEAS-2B cells and 20 μg/mL for *E. coli* in downstream experiments. Of note, human gDNA did not show any impact on MBP-$1_{18–45}$-induced cell death on either bacterial or human cells, independent of its concentration (Figures 1C and 1D).

Next, we assessed bacterial killing and BEAS-2B cell death after 1 h of treatment with either MBP-$1_{18–45}$ alone or in combination with mtDNA, bacterial DNA, and human gDNA (Figures 1E and 1F). Notably, our findings demonstrated that mtDNA significantly amplified the toxicity mediated by MBP-$1_{18–45}$ in both *E. coli* and BEAS-2B cells, closely resembling the effect of bacterial DNA (Figures 1E and 1F). Importantly, we did not observe a similar effect in combination with human gDNA (Figures 1E and 1F). Bacterial DNA, mtDNA, and human gDNA individually exhibited no signs of toxicity in *E. coli* and BEAS-2B cells when administered alone (Figures 1E and 1F). Thus, the increased toxicity observed upon combined treatment of MBP-$1_{18–45}$ with bacterial DNA or mtDNA likely arises from the interaction between MBP-1 and both DNAs rather than stemming from a cumulative effect of their individual toxicities. These findings underscore the role of mtDNA in EETs and propose a regulatory function for mtDNA in modulating the toxicity of MBP-1.

We have recently shown the neutralization of MBP-1-mediated toxicity toward host cells with heparin, a known enhancer of amyloid aggregation that leads to the formation of long, non-toxic MBP-1 fibrils.[20] We confirmed that heparin significantly reduced MBP-$1_{18–45}$-induced cell death in BEAS-2B cells (Figure 1F). Interestingly, heparin increased the antibacterial activity of MBP-$1_{18–45}$ to a similar extent as bacterial DNA (Figure 1E), which could indicate how different aggregation products have species-specific toxicity.

Next, we assessed bacterial killing and BEAS-2B viability kinetics in a time-dependent manner (Figures 1G and 1H). MBP-$1_{18–45}$ toxicity progressively increased over time, following a linear trend, which eventually plateaued approximately after 1 h of treatment (Figures 1G and 1H). In the presence of bacterial DNA, the bactericidal activity of MBP-$1_{18–45}$ reached its highest level within the first 5 min (Figure 1G). Similarly, bacterial DNA accelerated MBP-$1_{18–45}$-mediated cell death in BEAS-2B cells, resulting in about 50% cell death within the first 5 min of treatment, followed by a decelerated incline up to 80% cell death after 1 h (Figure 1H). Furthermore, although human gDNA induced a similar rapid increase in MBP-$1_{18–45}$-mediated toxicity in *E. coli* within the first 5 min of treatment, its overall effect on bacterial viability was considerably lower, resembling that of MBP-$1_{18–45}$ alone (Figure 1G). The substantial molecular weight of human gDNA likely plays a role in accelerating the antimicrobial effect of MBP-$1_{18–45}$ by impeding bacterial mobility. This restriction may facilitate MBP-1's local action, thereby increasing its efficacy. We observed no differences in the kinetics of MBP-$1_{18–45}$-mediated cell death in BEAS-2B cells when treated in combination with human gDNA (Figure 1H). As shown previously, heparin effectively counteracted the toxic effects of MBP-$1_{18–45}$ on BEAS-2B cells (Figure 1H) while leading to a significant increase in the toxicity of MBP-$1_{18–45}$ toward bacteria, similarly to bacterial DNA (Figure 1G).

Influence of CpG DNA methylation status on MBP-1-mediated toxicity

The toxicity of MBP-1 was highly influenced by the presence of mtDNA (Figures 1E and 1F). This interaction is also found *in vivo* within the formation of EETs, where the negatively charged mtDNA acts as a scaffold to trap microorganisms while concentrating positively charged granule proteins.[19] We stained isolated primary eosinophils from the peripheral blood of mice genetically modified to express GFP-tagged mitochondria with Hoechst 33342 to visualize the nucleus and MitoSOX Red to detect mitochondrial extracellular DNA.[44] Next, we co-cultured BEAS-2B cells with the eosinophils primed with granulocyte-macrophage colony-stimulating factor (GM-CSF) and activated with complement component 5a (C5a).[45] Prior to co-culture, we stained the BEAS-2B cells with Hoechst 33342 and CellTracker Deep Red. Using live-cell confocal microscopy, we monitored the *in vitro* formation of EETs (Figure 2A). Our observations revealed the presence of viable eosinophils with mitochondria translocated to the plasma membrane, releasing mtDNA into the extracellular space. This mtDNA trap was observed to extend across and covering a portion of the plasma membrane of a BEAS-2B cell. Additionally, BEAS-2B cells displayed signs of cell death within 1 h of co-culture with GM-CSF-primed and C5a-activated eosinophils.

Remarkably, mtDNA has been reported previously to exhibit low CpG methylation levels similar to bacterial DNA[46,47] and could induce a similar enhancement in MBP-1-mediated toxicity (Figures 1E–1H). We confirmed CpG methylation status of mtDNA and bacterial DNA in our samples, which showed comparably low methylation in contrast to the highly methylated nature of human gDNA (Figure 2B). To elucidate the potential role of CpG DNA methylation on the toxicity of MBP-1, we artificially introduced methylation in bacterial DNA (*m*bacterial DNA) through the overexpression of the gene encoding for DNA methyltransferase in *E. coli* (Figure 2B). Moreover, we reversed the CpG island methylation in human gDNA (*dm*human gDNA) using the DNA methyltransferase inhibitor 5-aza-2′-deoxycytidine (5-aza-2′-CdR) (Figure 2B). Interestingly, *m*bacterial DNA displayed a negligible impact on MBP-$1_{18–45}$–mediated toxicity toward both *E. coli* and BEAS-2B cells, analogous to the responses observed with human gDNA (Figures 2C and 2D). In contrast, *dm*human gDNA significantly elevated the toxicity mediated by MBP-$1_{18–45}$, similar to bacterial DNA (Figures 2C and 2D). Taken together, these findings emphasize the involvement of CpG DNA methylation in the modulation of MBP-1 toxic effects.

Rapid membrane permeabilization in MBP-1-treated human bronchial epithelial cells

Although being recognized for its toxicity toward mammalian cells for several years,[41] the specific type of cell death induced by MBP-1 remains largely unexplored. To clarify the MBP-1-mediated cell death mechanism, we used a number of distinct pharmacological inhibitors targeting various forms of cell death, including apoptosis, necroptosis, pyroptosis, ferroptosis, and parthanatos, as well as inhibitors that affect cellular processes such as ROS production, cytoskeletal

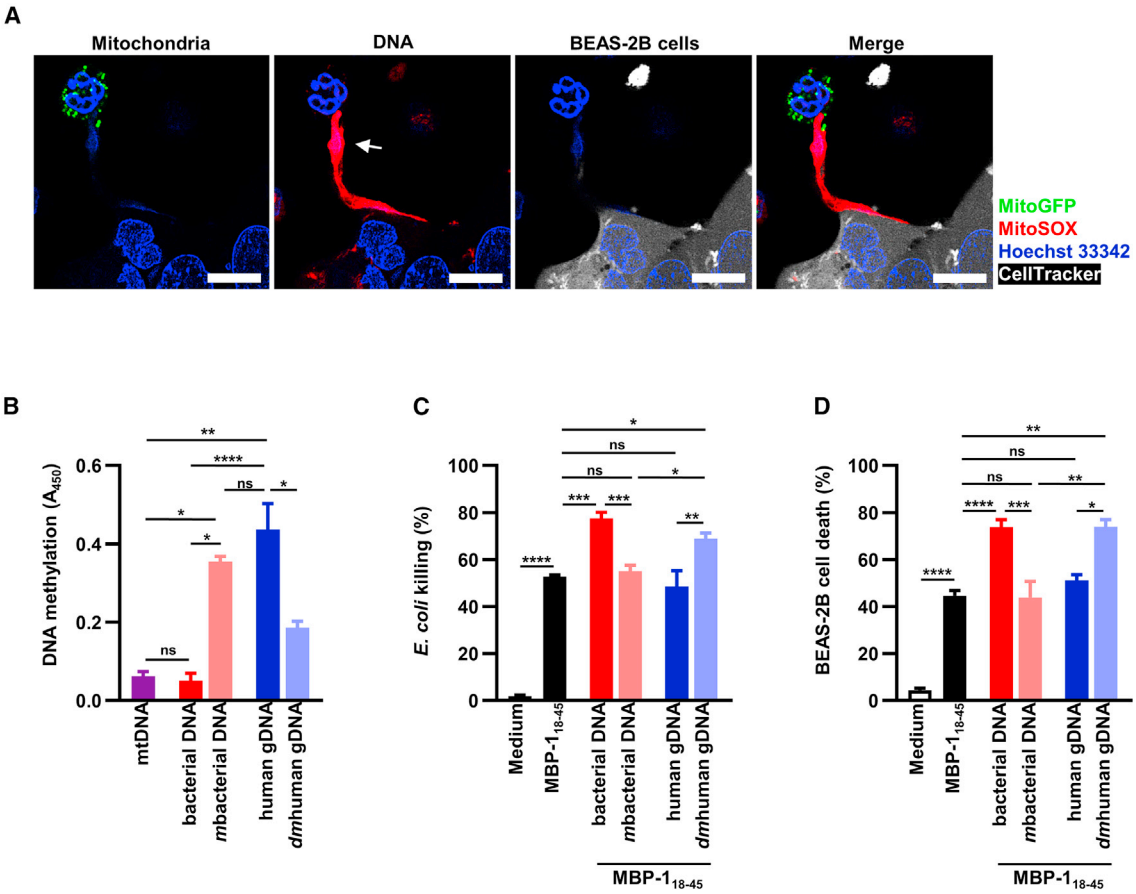

Figure 2. Toxicity toward microorganisms and mammalian cells mediated by MBP-$1_{18–45}$ in combination with methylation-modified DNA

(A) Mouse peripheral blood eosinophils with stable expression of MitoGFP (green) were stained with Hoechst 33342 (blue) and MitoSOX (red). BEAS-2B cells were stained with Hoechst 33342 (blue) and CellTracker Deep Red (white). Eosinophils were primed with GM-CSF and co-cultured with BEAS-2B cells before activation with C5a. An arrow indicates the released mtDNA. Scale bars, 10 μm. Images are representative of 2 technical replicates with 2 culture replicates.

(B) 5-methylcytosine (5mC) methylation of mtDNA, bacterial DNA, methylated bacterial (*m*bacterial) DNA, human gDNA, and demethylated human (*dm*human) gDNA was analyzed using an ELISA. Data are representative of 3 independent biological replicates.

(C and D) Viability assay. *E. coli*-GFP (C) and BEAS-2B cells (D) were treated with MBP-$1_{18–45}$ in the presence or absence of bacterial DNA, *m*bacterial DNA, human gDNA, and *dm*human gDNA for 1 h. Cell toxicity was assessed by the loss of GFP (C) or the uptake of PI (D) using flow cytometry. Data are representative of 3 independent biological replicates. The assays were performed in duplicates.

All data are represented as mean ± SEM, and *p* values (*$p < 0.05$, **$p < 0.01$, ***$p < 0.001$, ****$p < 0.0001$) were calculated using ordinary one-way ANOVA with Tukey's multiple comparisons (B–D).

rearrangement, and glycolysis (Figure S1; Table S1). None of the agents tested could inhibit MBP-$1_{18–45}$-mediated cell death (Figure S1). Next, we set out to perform live-cell imaging by confocal microscopy to better understand the process of cell death mediated by MBP-1. We stained BEAS-2B cells with the viable cell indicator calcein AM and cell death indicator ethidium homodimer 1 as well as Hoechst 33342 to visualize the nuclei (Figure 3A). Within a time span of 15 min in the presence of MBP-$1_{18–45}$, BEAS-2B cells exhibited noticeable shrinkage (Figure 3A). After 30 min, we observed the release of calcein from the cells and a decrease in fluorescence intensity of Hoechst 33342 followed by the uptake of ethidium homodimer 1 in the nuclei, indicating nuclear membrane permeabilization approximately 40–50 min after the addition of MBP-$1_{18–45}$ (Figure 3A). These observations are consistent with the prior finding that MBP-1 exerts its effects on membranes, leading to their disruption.[20,22]

To investigate the specific form of membrane damage caused by MBP-1, we explored the impact of punicalagin, a recognized inhibitor of plasma membrane permeabilization,[48] and glycine, a known inhibitor of plasma membrane rupture,[49] on the toxicity induced by MBP-$1_{18–45}$ toward BEAS-2B cells (Figure 3B). Punicalagin significantly reduced the toxicity of MBP-$1_{18–45}$ even in combination with mtDNA (Figure 3B). In contrast, no effect on MBP-$1_{18–45}$-mediated toxicity was observed with glycine (Figure 3B). Plasma membrane permeabilization entails changes to the membrane's integrity without complete disruption of the lipid bilayer, enabling the uncontrolled passage of molecules and ions.[50] In contrast, plasma membrane rupture involves the complete breakdown of the cell membrane, leading to irreversible

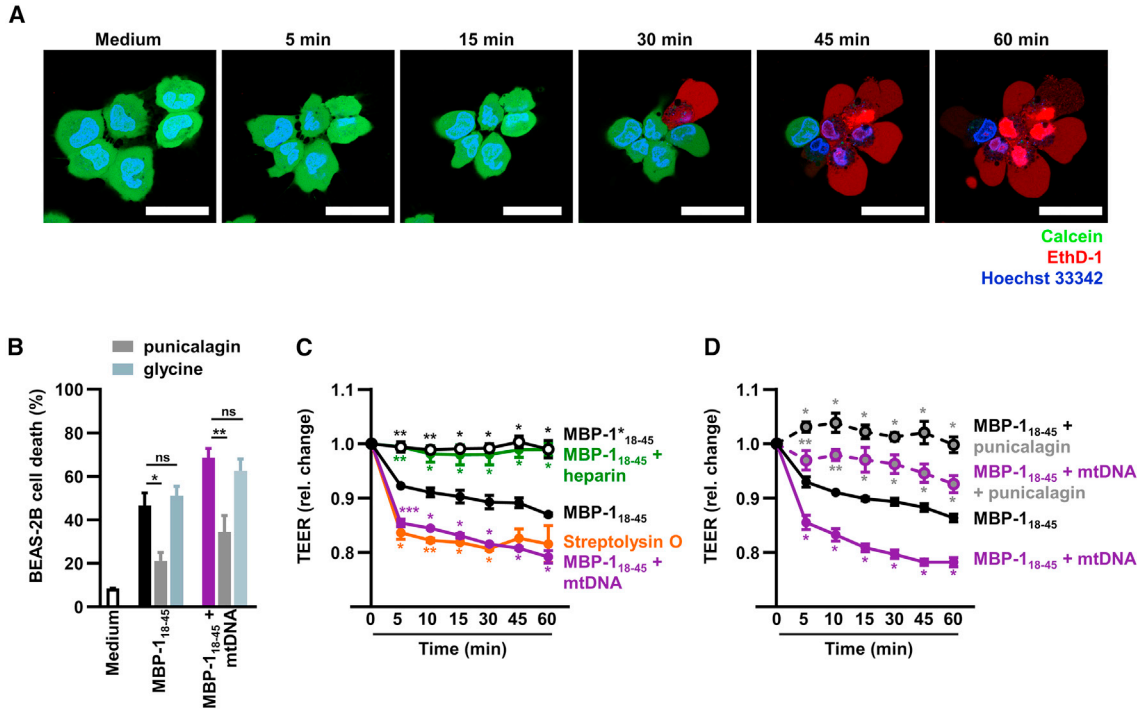

Figure 3. Time-dependent permeabilization of the plasma membrane mediated by MBP-$1_{18–45}$

(A) BEAS-2B cells were treated with MBP-$1_{18–45}$ for the indicated times. The cells were stained with Hoechst 33342 (blue), calcein AM (green), and ethidium homodimer 1 (red) to determine cell viability using live-cell confocal microscopy. Scale bars, 40 μm. Images are representative of 3 independent biological replicates.

(B) BEAS-2B cells were pretreated with punicalagin (50 μM) or glycine (5 mM) for 30 min before treatment with MBP-$1_{18–45}$ in the presence or absence of mtDNA. Cell toxicity was assessed by the uptake of PI using flow cytometry. Data are representative of 3 independent biological replicates. The assay was performed in duplicates.

(C and D) BEAS-2B cells were pretreated with punicalagin (50 μM) for 30 min before treatment with MBP-$1_{18–45}$ in the presence or absence of mtDNA. Heparin and MBP-$1^*_{18–45}$ were used as negative controls. SLO was used as a positive control. Transepithelial electrical resistance (TEER) was measured across epithelial monolayers at the indicated time points. TEER values are shown as fold change to untreated cells. Significances are shown against MBP-$1_{18–45}$ alone (black) or, in the case of punicalagin, against the corresponding condition. Data are representative of 3 independent biological replicates.

All data are represented as mean ± SEM, and p values ($p < 0.05$, $^{**}p < 0.01$, $^{***}p < 0.001$) were calculated using ordinary one-way ANOVA with Tukey's multiple comparisons (B) and two-way ANOVA with Dunnett's multiple comparisons (C) or Tukey's multiple comparisons (D).

damage.[51] To confirm the impact of MBP-$1_{18–45}$ on membrane permeability, we performed transepithelial electrical resistance (TEER) measurements in BEAS-2B cells (Figures 3C and 3D). We observed decreased electrical resistance over time upon the addition of MBP-$1_{18–45}$, confirming membrane permeabilization (Figure 3C). Moreover, the reduction occurred immediately upon addition of MBP-$1_{18–45}$, indicating a rapid action of MBP-$1_{18–45}$ on the plasma membrane. The reduction in electrical resistance was significantly more profound with MBP-$1_{18–45}$ in combination with mtDNA (Figure 3C). Interestingly, this reduction was comparable with the decrease in electrical resistance observed with the addition of streptolysin O (SLO), a bacterial pore-forming toxin.[52] The addition of heparin rescued the decrease in electrical resistance (Figure 3C), which was in line with our previous finding that heparin neutralizes MBP-1-mediated toxicity on human cells (Figures 1F and 1H). Punicalagin significantly decreased the permeabilization of the plasma membrane induced by MBP-$1_{18–45}$ alone or together with mtDNA (Figure 3D), in accordance with the observed reduction in toxicity (Figure 3B).

MBP-1-mediated membrane damage in human bronchial epithelial cells

Scanning electron microscopy imaging revealed the formation of ring-like structures (yellow dashed lines) composed of MBP-$1_{18–45}$ aggregates binding to the plasma membrane of BEAS-2B cells, causing evident membrane damage (red dotted lines) within these formations (Figure 4A). These aggregates started to form as early as 10 min after MBP-$1_{18–45}$ treatment and grew in size over time (Figure S2A). Moreover, the extent of membrane damage increased progressively over time (Figures 4A and S2). While the ring structures of MBP-$1_{18–45}$ aggregates (yellow dashed lines) remained largely unaffected in the presence of heparin and punicalagin, the integrity of the membrane was preserved, thus validating the protective effect of these two agents (Figure 4A).

Consistently, transmission electron microscopy (TEM) of BEAS-2B cells revealed membrane damage in close proximity to MBP-$1_{18–45}$ aggregates (Figures 4B and 4C). The extent of the damage induced by MBP-$1_{18–45}$ significantly increased over time (Figure 4B), following a similar trend as observed in

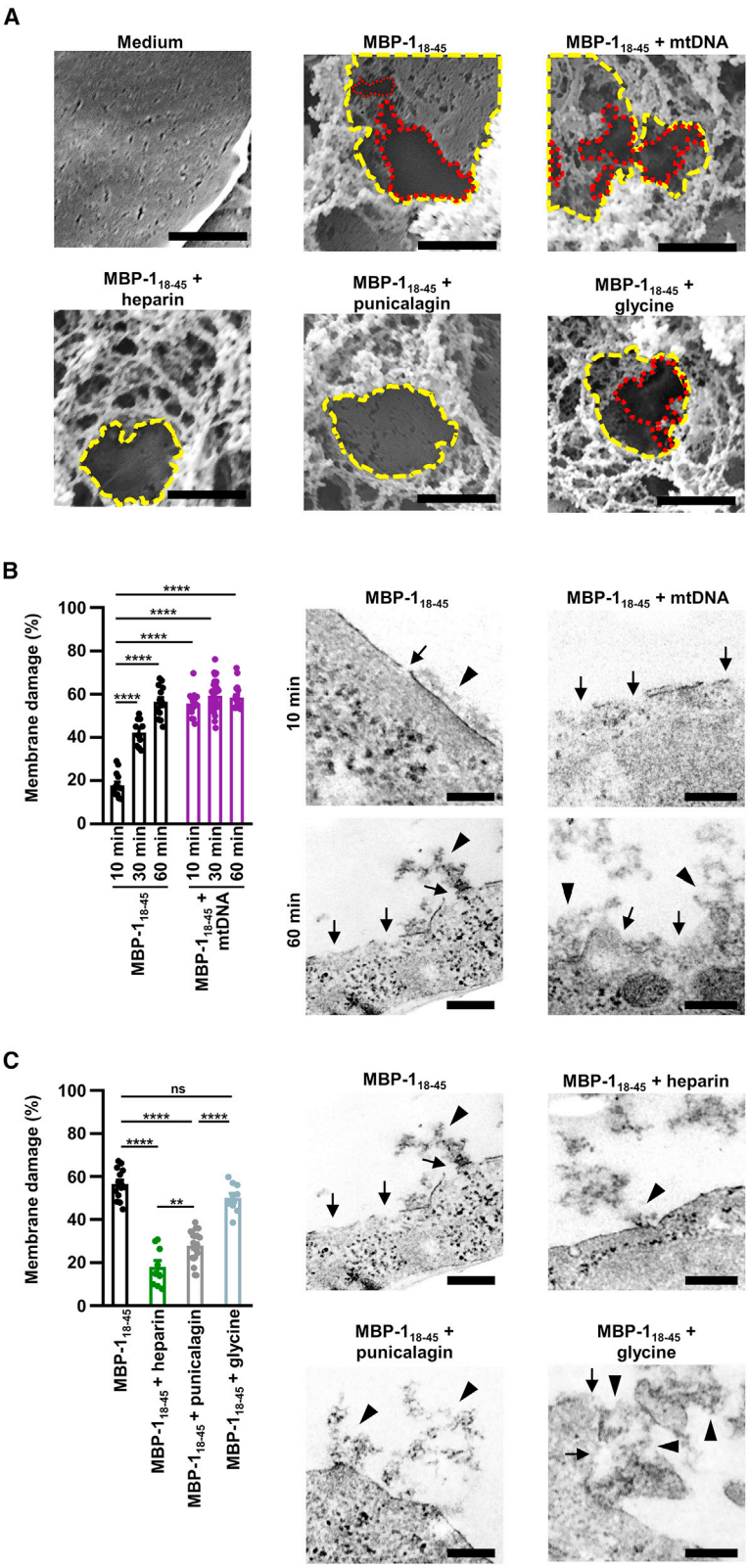

Figure 4. Plasma membrane damage in MBP-$1_{18–45}$-treated human bronchial epithelial cells

(A) BEAS-2B cells were pretreated with punicalagin (50 μM) or glycine (5 mM) for 30 min before treatment with MBP-$1_{18–45}$ in the presence or absence of mtDNA for 1 h. Heparin was used as a negative control. The cells were fixed and analyzed by scanning electron microscopy. Yellow dashed lines indicate the ring-like structures of MBP-$1_{18–45}$ peptide aggregates. Red dotted lines indicate the area with membrane damage within the ring-like structures of MBP-$1_{18–45}$ peptide aggregates. Scale bars, 1 μm. Images are representative of 2 independent biological replicates.

(B and C) BEAS-2B cells were pretreated with punicalagin (50 μM) or glycine (5 mM) for 30 min for the indicated conditions before treatment with MBP-$1_{18–45}$ in the presence and absence of mtDNA for 1 h. Heparin was used as a negative control. The cells were fixed and analyzed by TEM. Left: quantification of the plasma membrane damage. Sums of membrane damage are normalized to the length of the plasma membrane shown. Each dot represents a single cell. Right: arrows indicate membrane damage. Arrowheads indicate MBP-$1_{18–45}$ peptide aggregates. Scale bars, 250 nm. Images are representative of 2 independent biological replicates.

All data are represented as mean ± SEM, and p values (**$p < 0.01$, ****$p < 0.0001$) were calculated using ordinary one-way ANOVA with Tukey's multiple comparisons (B and C). See also Figure S2.

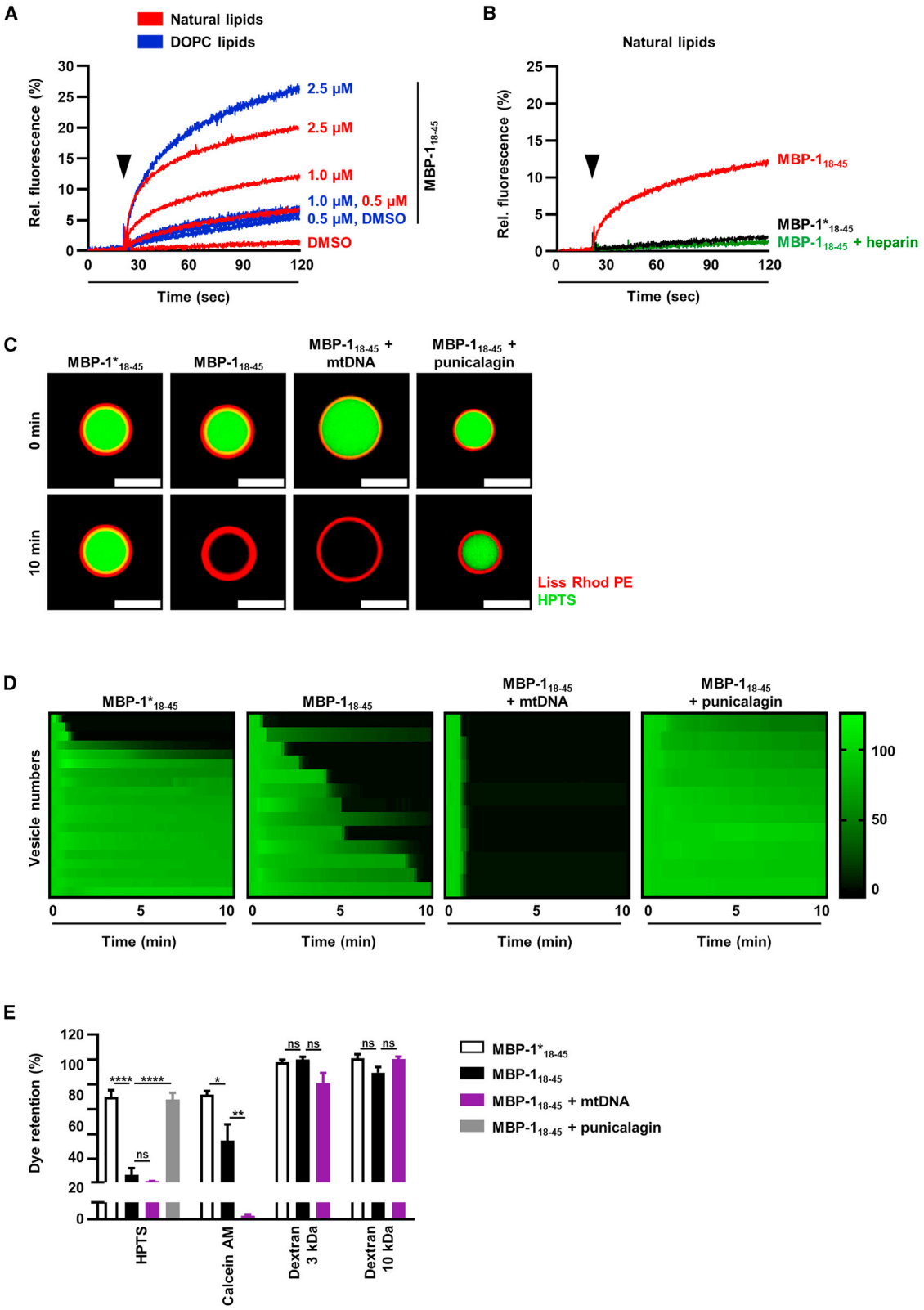

(legend on next page)

MBP-$1_{18–45}$-mediated death of BEAS-2B cells (Figure 1H). The addition of mtDNA caused a significantly higher degree of membrane damage within 10 min of treatment compared with MBP-$1_{18–45}$ treatment alone (Figure 4B). These findings align with previous results that demonstrated increased toxicity (Figures 1F and 1H) as well as elevated membrane permeabilization (Figure 4C) induced by MBP-$1_{18–45}$ in combination with mtDNA, particularly during the early time points. Furthermore, the membrane damage induced by MBP-$1_{18–45}$ was significantly reduced by heparin (Figure 4C), consistent with the reduced toxicity observed in BEAS-2B cells (Figures 1F and 1H). Punicalagin led to significantly decreased membrane damage in contrast to glycine (Figure 4C), which correlates with the diminished toxic effect of MBP-$1_{18–45}$ in punicalagin-pretreated BEAS-2B cells (Figure 3B). Taken together, we confirm that MBP-1 induces damage to the plasma membrane, leading to its permeabilization, a process that is accelerated by mtDNA.

Formation of small pores by MBP-1 in lipid bilayers

To understand the minimal requirements for membrane damage induced by MBP-$1_{18–45}$, we investigated the leakage of 5(6)-carboxyfluorescein (CF) from liposomes that mimic the composition of mammalian plasma membranes[53] (natural lipids) and 1,2-dioleoyl-*sn-glycero*-3-phosphochline (DOPC) liposomes after addition of MBP-$1_{18–45}$. MBP-$1_{18–45}$ prompted an immediate and concentration-dependent leakage of CF from natural liposomes (Figure 5A), resembling the concentration-dependent cytotoxic effect of MBP-$1_{18–45}$ on BEAS-2B cells (Figure 1B). CF release from natural liposomes was not observed in combination with heparin or with MBP-$1^*_{18–45}$ (Figure 5B). These findings confirm the interaction of MBP-1 with lipid bilayers and suggest that its aggregation is a prerequisite for its action on the cell membrane. It's worth noting that DOPC liposomes possessing an overall neutral charge displayed a comparable release of CF when exposed to 2.5 μM MBP-1_{18-45} (Figure 5A). In contrast, at lower concentrations (1 and 0.5 μM) of MBP-$1_{18–45}$, no CF release was induced in DOPC liposomes. These findings imply that, although MBP-1 has a toxic impact on both types of liposomes, it demonstrates greater efficacy in disrupting lipid bilayers comprised of natural lipid compositions compared with those with a neutral composition.

To shed light on the specific nature of membrane damage, we studied the release of 8-hydroxypyrene-1,3,6-trisulfonic acid, trisodium salt (HPTS) from giant unilamellar vesicles (GUVs) mimicking the composition of mammalian cell membrane[53] using confocal fluorescence microscopy (Figure 5C). We demonstrated that the addition of MBP-$1_{18–45}$, alone as well as in combination with mtDNA, leads to the complete loss of dye after 10 min, while MBP-$1^*_{18–45}$ caused no dye leakage (Figure 5C). Furthermore, the GUV membrane, stained using fluorescently labeled lipids, remained largely intact during the leakage process (Figure 5C), indicating that the leakage of dye was attributed to the formation of discrete pores in the membrane rather than an overall loss of integrity. In line with the previous results, punicalagin significantly reduced the dye loss (Figures 5C and 5D). The kinetics of dye leakage showed how mtDNA significantly accelerated the release of HPTS from the vesicles (Figure 5D).

To approximate the size of the formed pore, we assessed the release of distinct dyes with various molecular weights from GUVs (Figure 5E). MBP-$1_{18–45}$ led to the complete loss of HPTS (0.5 kDa) and partial release of calcein (0.6 kDa) after 10 min, while 3 kDa and 10 kDa dextrans remained trapped inside the GUVs (Figure 5E). Notably, the presence of mtDNA not only induced significant increased leakage of calcein upon MBP-$1_{18–45}$ treatment (Figure 5E) but also accelerated its release (Figures S3A and S3B). Alamethicin, a fungal pore-forming peptide,[54] induced release of the 10 kDa dextran, acting as a positive control (Figure S3C). These findings collectively suggest that the pores created by MBP-$1_{18–45}$ are relatively small in size, with a molecular weight permeability threshold of approximately 1 kDa (Figure 5E).

Interaction of MBP-1 with lipid bilayers

Cryoelectron microscopy (cryo-EM) has emerged as a powerful tool for elucidating the structural aspects of pores formed by a wide array of proteins.[55,56] Consequently, we employed cryo-EM to gain more detailed insight into the process of pore formation by MBP-1, exposing liposomes mimicking plasma membrane lipid composition[53] to MBP-$1_{18–45}$ treatment (Figure 6). We observed a number of liposomes with disrupted lipid bilayers (arrows) (Figure 6A), confirming the findings from the CF leakage experiments (Figure 5D). Moreover, we identified larger

Figure 5. Pore formation by MBP-1_{18-45} in liposomes

(A and B) Natural liposomes (total soy extract, total liver extract, cholesterol, and sphingomyelin; 4:4:1:1 ratio) and neutral liposomes (DOPC) were treated with the indicated concentrations of MBP-$1_{18–45}$. DMSO, MBP-$1^*_{18–45}$, and heparin were used as negative controls. Liposomes were loaded with CF, and dye leakage was analyzed using a PTI fluorescence spectrophotometer. Arrowheads indicate the addition of peptide or DMSO after 20 s. Fluorescence was normalized to maximal fluorescence after complete solubilization of liposomes with Triton X-100. Data are representative of 2 independent biological replicates.

(C–E) GUVs (total soy extract, total liver extract, cholesterol, and sphingomyelin; 4:4:1:1 ratio) were pretreated with punicalagin (50 μM) for 30 min before treatment with 2.5 μM MBP-$1_{18–45}$ in the presence or absence of mtDNA for 10 min. MBP-$1^*_{18–45}$ was used as a negative control. GUVs were loaded with fluorescent dyes, and dye leakage was observed using inverted fluorescence imaging. Data and images are representative of 13 (MBP-$1_{18–45}$, HPTS), 20 (MBP-$1^*_{18–45}$, HPTS; MBP-$1_{18–45}$, 10 kDa), 8 (MBP-$1_{18–45}$ + mtDNA, HPTS), 10 (MBP-$1_{18–45}$ + punicalagin, HPTS; MBP-$1_{18–45}$, calcein), 7 (MBP-$1^*_{18–45}$, calcein), 12 (MBP-$1_{18–45}$ + mtDNA, calcein), 9 (MBP-$1_{18–45}$, 3 kDa; MBP-$1_{18–45}$ + mtDNA, 3 kDa), 21 (MBP-$1^*_{18–45}$, 3 kDa), 14 (MBP-$1^*_{18–45}$, 10 kDa), and 5 (MBP-$1_{18–45}$ + mtDNA, 10 kDa) technical replicates of GUV dye leakage.

(C) GUVs are visualized using Liss Rhod PE (red) and encapsulated with HPTS (green). Scale bars, 10 μm.

(D) Dye leakage over time of GUVs encapsulating HPTS is presented as heatmaps. Color corresponds to fluorescence intensity as percentage that is retained in the lumen of the GUVs. GUVs are ordered according to the time point when 50% leakage was observed.

(E) GUVs encapsulated either HPTS, calcein AM, Texas Red 3,000 molecular weight (MW) dextran, or Texas Red 10,000 MW dextran. Dye leakage is represented as the endpoint measurement after 10 min of treatment. Fluorescence was normalized to maximal fluorescence before MBP-$1_{18–45}$ addition.

All data are represented as mean ± SEM, and *p* values (**p* < 0.05, ***p* < 0.01, *****p* < 0.0001) were calculated using ordinary one-way ANOVA with Tukey's multiple comparisons (E). See also Figure S3.

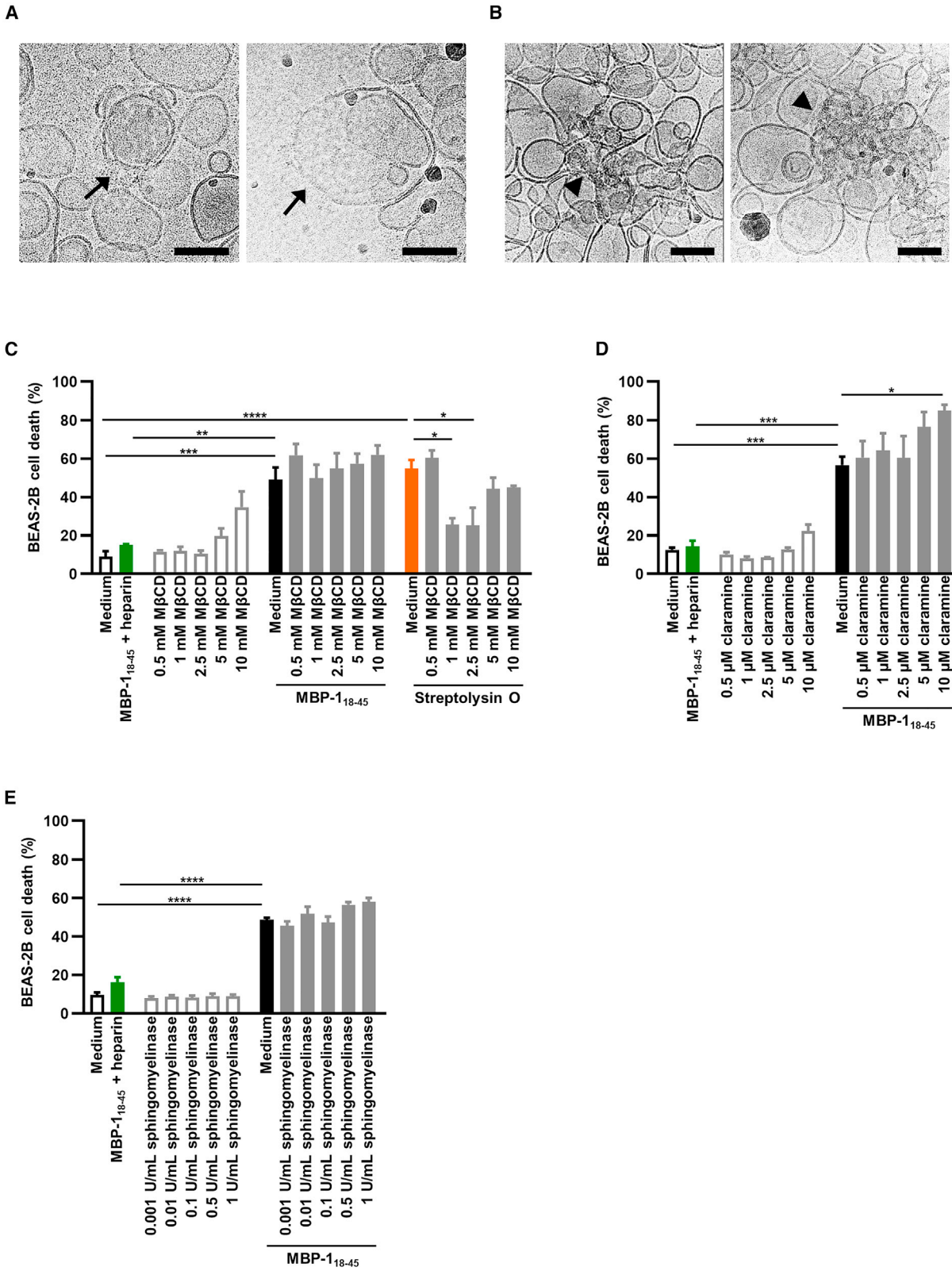

(legend on next page)

aggregates of MBP-$1_{18–45}$ extending across multiple liposomes (Figure 6B). Within these groups of liposomes, evidence of disruption of the bilayers was also detected (Figure 6B, arrowheads). However, we did not uncover a distinct pore structure adjacent to these lipid disruptions (Figure 6A), likely due to its anticipated small size of approximately less than 1 kDa of leakage molecule size (Figure 5C).

While previous studies have demonstrated the impact of MBP-1 on the membranes of diverse organisms,[20,22,57] the precise mechanism of these interactions remains largely unidentified. Cholesterol plays a crucial role in the structure and function of eukaryotic cell membranes.[58] Moreover, it acts as an interaction partner for several pore-forming mediators; for example, amyloid proteins such as β-amyloid and α-synuclein[59] or proteins of the cholesterol-dependent cytolysin (CDC) family.[60,61] Thus, we depleted cholesterol from the plasma membrane of BEAS-2B cells by adding methyl-β-cyclodextrin (MβCD) for 1 h before treatment with MBP-$1_{18–45}$ (Figure 6C). SLO, belonging to the CDC family,[60,61] exerts its cytotoxic effect through its binding to cholesterol in mammalian cell membranes.[62] This interaction triggers the oligomerization of SLO, resulting in the formation of pores and, finally, cell lysis.[63] We observed a significant increase in BEAS-2B cell death upon treatment with SLO that was significantly reduced upon pretreatment with 1 mM and 2.5 mM MβCD (Figure 6C), confirming the depletion of cholesterol from the plasma membrane. However, various concentrations of MβCD (0.5–10 mM) exhibited no effect on MBP-$1_{18–45}$-mediated toxicity toward BEAS-2B cells (Figure 6C).

Aminosterols have been recognized recently for their ability to prevent toxicity of some pore-forming toxins by integrating into the membrane.[64] This incorporation resulted in a less negative charge of the membrane, along with a redistribution of cholesterol and ganglioside GM1 molecules.[64] Pretreatment with various concentrations of claramine trifluoroacetate salt (0.5–10 μM) for 30 min failed to confer protection for BEAS-2B cells against MBP-$1_{18–45}$ (Figure 6D). Interestingly, the highest concentration of claramine trifluoroacetate salt employed (10 μM) amplified MBP-$1_{18–45}$-mediated toxicity (Figure 6D).

Apart from cholesterol, sphingomyelin is prevalent in lipid rafts, playing a crucial role as an interaction partner for various pore-forming toxins.[65,66] However, after administrating sphingomyelinase (0.001–1 U/mL) for 1 h to BEAS-2B cells to deplete sphingomyelin from the plasma membrane, there was no observed reduction of MBP-$1_{18–45}$-mediated toxicity (Figure 6E).

Collectively, these findings confirm that membrane charge has little effect on MBP-1 toxicity and that neither cholesterol nor sphingomyelin is a crucial interaction partner to anchor MBP-1 to membranes. This is largely expected due to our demonstrated effects of MBP-1 in cholesterol-free bacterial membranes[20] (Figures 1A, 1C, 1E, and 1G), which further emphasizes the broad ability of MBP-1 to interact with bilayers of diverse composition to elicit permeabilization.

Impact of MBP-1 on cellular ion homeostasis

The formation of pores in cell membranes has the potential to significantly impact cellular ion concentrations, thereby disturbing their equilibrium and potentially resulting in cellular dysfunction.[50] To investigate this phenomenon, we examined the intracellular levels of potassium and calcium during the course of MBP-$1_{18–45}$ treatment (Figure 7).

Using the potassium-specific dye IPG-1, we observed a significant reduction in intracellular potassium levels within BEAS-2B cells as early as 10 min into the treatment with MBP-$1_{18–45}$ (Figure 7A). Additionally, the presence of mtDNA further contributed to the reduction in potassium concentration during the initial 10 min of treatment (Figure 7A). In agreement with its protective effect on MBP-$1_{18–45}$-mediated toxicity against BEAS-2B cells (Figure 1F), heparin completely inhibited the induced potassium efflux (Figure 7A).

To assess the intracellular calcium levels, we employed Fluo-3 staining in combination with live-cell confocal microscopy (Figure 7B). In contrast to the observed decrease in intracellular potassium levels (Figure 7A), we did not detect any apparent calcium influx in BEAS-2B cells in response to MBP-$1_{18–45}$ (Figure 7B). Similarly, the presence of mtDNA did not lead to elevated levels of intracellular calcium in BEAS-2B cells when exposed to MBP-$1_{18–45}$ (Figure 7B). On the other hand, ionomycin, a well-known Ca^{2+} ionophore,[67] induced a significant increase in intracellular calcium concentration (Figure 7B). Collectively, our findings demonstrate that MBP-1 initiates a rapid potassium efflux, disrupting the cellular ion homeostasis in human bronchial epithelial cells.

DISCUSSION

The antibacterial activity of MBP-1 was discovered decades ago,[22] alongside its cytotoxic properties and involvement in allergic, infectious, and autoimmune diseases.[23,41] We have demonstrated previously that the regulation of MBP-1 toxicity encompasses its crystallization inside the eosinophil itself as well as its amyloidogenic aggregation in the extracellular space.[20] However, the precise mechanism by which MBP-1 exerts its toxicity remains largely elusive.

Figure 6. Characterization of MBP-1 interaction with lipid bilayers

(A and B) Liposomes (total soy extract, total liver extract, cholesterol, and sphingomyelin; 4:4:1:1 ratio) were treated with 1 μM MBP-$1_{18–45}$ for 20 min. The liposomes were deposited onto a copper grid, plunged into liquid ethane, and analyzed by TEM. Arrows indicate perturbations to the lipid bilayer of liposomes. Arrowheads indicate MBP-$1_{18–45}$ peptide aggregates. Scale bars, 100 nm. Images are representative of 3 independent biological replicates.

(C–E) BEAS-2B cells were pretreated with the indicated concentrations of methyl-β-cyclodextrin (MβCD) (0.5–10 mM) for 1 h, claramine trifluoramine acid (0.5–10 μM) for 30 min, or sphingomyelinase (0.001–1 U/mL) for 1 h, followed by treatment with MBP-$1_{18–45}$ for 1 h. Heparin was used as a negative control. SLO was used as a positive control. Cell toxicity was assessed by the uptake of PI using flow cytometry. Data are representative of 3 independent biological replicates. The assays were performed in duplicates.

All data are represented as mean ± SEM, and p values (*$p < 0.05$, **$p < 0.01$, ***$p < 0.001$, ****$p < 0.0001$) were calculated using ordinary one-way ANOVA with Tukey's multiple comparisons (C–E).

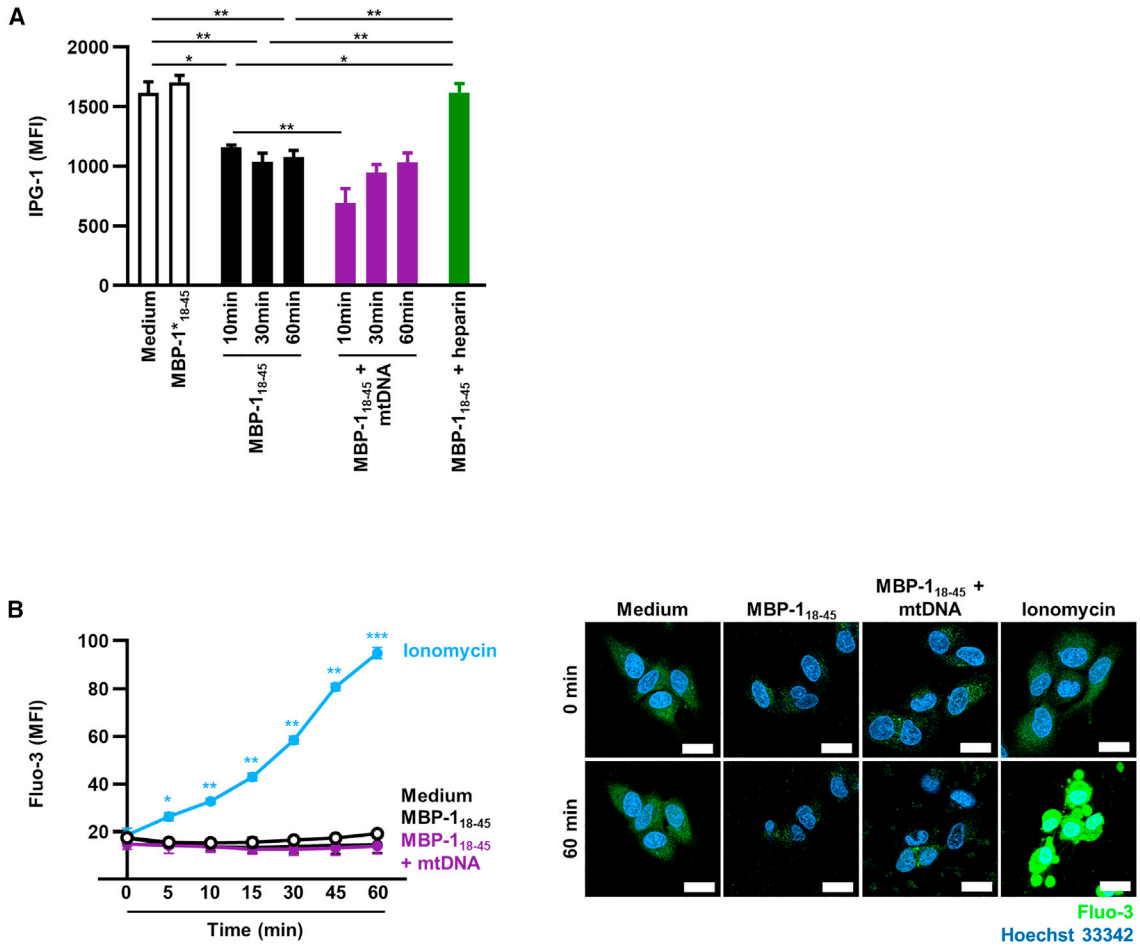

Figure 7. Changes in ion concentrations in MBP-$1_{18–45}$-treated human bronchial epithelial cells

(A) BEAS-2B cells were treated with MBP-$1_{18–45}$ in the presence and absence of mtDNA for the indicated time. Heparin was used as a negative control. The cells were stained with IPG-1 AM and potassium concentration was assessed using flow cytometry. Data are representative of 3 independent biological replicates. The assay was performed in duplicates.

(B) BEAS-2B cells were stained with Fluo-3 AM (green) and Hoechst 33342 (blue) and analyzed immediately upon treatment with MBP-$1_{18–45}$ in the presence or absence of mtDNA using live-cell confocal microscopy. Ionomycin was used as a positive control. Left: quantification of the calcium levels was performed by automated analysis of microscopy images using Imaris software. Significances are shown against MBP-$1_{18–45}$ alone (black). Right: bars, 20 μm. Data are representative of 3 independent biological replicates. The assay was performed in duplicates.

All data are represented as mean ± SEM, and p values (*$p < 0.05$, **$p < 0.01$, ***$p < 0.001$) were calculated using ordinary one-way ANOVA with Tukey's multiple comparisons (A) and two-way ANOVA with Dunnett's multiple comparisons (B).

In this study, we confirmed that MBP-1 toxicity arises from self-aggregation, as demonstrated by a control peptide with reduced aggregation propensity[20] (Figures 1A and 1B). On the other hand, the formation of large fibrils by heparin neutralizes the toxic capacity of MBP-1 against BEAS-2B cells (Figure 1F) while increasing the antibacterial properties of MBP-1 (Figure 1E). In our previous work, we demonstrated that MBP-1-induced toxicity is attributed to prefibrillar and fibrillar oligomers.[20] In contrast, for other amyloid proteins, toxicity is linked to the presence of fibrils.[68] The variation in how heparin affects MBP-1-induced toxicity toward mammalian cells and bacteria may serve as a host defense mechanism, potentially eliminating invading bacteria while protecting the surrounding host tissue. We have reported previously that MBP-1 induces a rapid cell death with morphological features resembling apoptosis but is unaffected by the pan-caspase inhibitor quinoline-Val-Asp-difluorophenoxymethylketone (Q-VD-OPh).[20] Using numerous pharmaceutical inhibitors against various effectors of cell death, including caspases, kinases, or poly(ADP-ribose) (PAR) polymerization, we demonstrate that the MBP-1 mechanism of action is distinct in that it does not induce any of the described regulated cell death types (Figure S1). Furthermore, previous findings have suggested that MBP-1 acts primarily on the very diverse membranes of microorganisms and mammalian cells, leading to their disruption and, ultimately, cell death.[20,22,57] Here, we demonstrate that MBP-1 induces permeabilization of the plasma membrane (Figure 3C), a process that can be significantly diminished by punicalagin (Figure 3D). However,

punicalagin does not entirely block the toxicity mediated by MBP-1 (Figure 3B), suggesting that the toxicity of MBP-1 might be more complex, possibly involving multiple modes of action. Additionally, BEAS-2B cells pretreated with punicalagin show a gradual decrease in electrical resistance, which initiates around 50–60 min into the MBP-1 treatment (Figure 3D), indicating that punicalagin might retard the membrane permeabilization induced by MBP-1 rather than achieving complete inhibition.

Disruption of the integrity of the cell membrane is often observed in the presence of amyloid proteins, antimicrobial peptides, or other pore-forming proteins, all of which possess the capability to initiate membrane permeabilization and pore formation.[59,69,70] Our data reveal that MBP-1 induces dye release from GUVs without visible disruption of the bilayer, indicating that MBP-1 exerts its action on the bilayer primarily through discrete pore formation (Figure 5C). Furthermore, by employing dyes of distinct molecular weights, we could estimate the approximate size of these pores to be about 1 kDa (Figure 5E). Cryo-EM analysis of liposomes treated with MBP-1 reveals small perturbations in the lipid bilayer, although the presence of a distinct pore structure is not evident, possibly due to the small pore size or membrane composition (Figures 6A and 6B). Interestingly, although the pore size of MBP-1 remains consistent in the presence of mtDNA (Figures 5E and S3), we observe notable differences in the speed of dye leakage (Figures 5D and S3). These findings suggest that mtDNA might augment the number of pores formed rather than altering their size, therefore leading to increased toxicity of MBP-1.

MBP-1 targets the membrane of various microorganism and mammalian cells,[9,22,41] demonstrating a clear, non-selective mode of action. Scanning electron microscopy imaging reveals the formation of MBP-1 ring-like structures on the surface of BEAS-2B cells (Figures 4A and S2). Notably, membrane damage predominantly occurs within these structures. Moreover, TEM analysis provides confirming evidence that the degree of membrane damage increases over time, similar to the documented cytotoxicity mediated by MBP-1 (Figure 4B). Importantly, we could observe a level of membrane damage comparable with 1 h treatment with MBP-1 within minutes of combined treatment with MBP-1 and mtDNA (Figure 4B), explaining the accelerated rate of toxicity observed in human cells and bacteria. Here, we demonstrate that neither changes nor redistribution of lipid composition in the plasma membrane of BEAS-2B cells affect the toxicity mediated by MBP-1 (Figures 6C and 6D). Notably, liposomes composed of more neutral charged lipids display evident variation in dye leakage when exposed to lower concentrations of MBP-1 (0.5–1 μM) in comparison with liposomes mimicking mammalian plasma membrane lipid composition (Figure 5A). These observations might suggest a role of negatively charged lipids in accelerating the destabilization of the lipid bilayer induced by MBP-1, although further experiments are needed to firmly establish this relationship.

Maintaining the integrity of the plasma membrane is a critical requirement to ensure the normal function and viability of cells. Any breach of integrity results in the unregulated passage of ions, molecules, and cellular components that ultimately result in cellular dysfunction and toxic effects.[69] Our data reveals that MBP-1 induces a rapid efflux of potassium in BEAS-2B cells (Figure 7A), which might be the leading cause of the striking observed shrinkage of the cells (Figure 3A). Potassium efflux is commonly linked to a decrease in cell volume due to osmotic adjustments[71] as well as alterations in membrane potential.[72,73] Likewise, numerous amyloidogenic proteins are associated with the disruption of membrane structural integrity, loss of critical ion gradients, and cell membrane depolarization.[74] In contrast, our findings suggest that the intracellular calcium levels remain unaffected by MBP-1 (Figure 7B). This outcome might be influenced by various factors, including the positively charged nature of MBP-1. However, further investigations are necessary to fully elucidate the impact and possible mechanisms of MBP-1 on intracellular calcium concentrations.

MBP-1 is also found in association with mtDNA as a part of the extracellular structures of EETs.[19] These structures are known to play a role in host defense[19] but also in the immunopathology of several eosinophil-associated diseases.[34] Previous studies have proposed that mtDNA acts as a scaffold, trapping microorganisms to facilitate the host defense action of granule proteins[34] while simultaneously limiting their impact to the trapped microorganism and protecting the surrounding host tissue.[34] Furthermore, mtDNA acts as a danger signal in mammalian cells due to its low level of CpG methylation and might therefore potentiate the immune response of granulocytes when extracellular traps are formed.[38] In this study, we show evidence that the mtDNA scaffold alters MBP-1 toxicity by amplifying and accelerating its impact on the viability of both bacteria (Figure 1E) and mammalian cells (Figure 1F). Moreover, this phenomenon is similarly observed with bacterial DNA but not human gDNA (Figures 1C–1F), indicating that low CpG DNA methylation levels play a pivotal role in the regulation of MBP-1 toxicity. Furthermore, enhanced methylation of bacterial DNA counteracts the augmenting effect on MBP-1, emphasizing that the absence of CpG DNA methylation is the key element behind the alteration of MBP-1-mediated toxicity (Figures 2C and 2D). Recent studies demonstrate that bacterial DNA enhances the neurotoxic effects of β-amyloid and tau protein by promoting and accelerating their amyloid aggregation,[42,75] indicating a possible shared mechanism involving non-methylated DNA in the aggregation of amyloidogenic proteins. It is important to note that, by verifying the salient role of mtDNA, but not human gDNA, in MBP-1-mediated cytotoxicity, our data add another line of evidence to the origin and mechanism of extracellular DNA composing EETs.

Collectively, our findings confirm that MBP-1 non-selectively targets pathogens and mammalian cells and therefore plays a role in both host defense and eosinophil-mediated immunopathology. Furthermore, our findings unveil an additional role of mtDNA within EETs, significantly amplifying MBP-1-mediated toxicity. In accordance with our data, *in vivo* evidence shows that EETs in eosinophilic diseases such as asthma are associated with increased inflammation.[76] Additionally, our study significantly contributes to the ongoing debate concerning the origin of DNA in extracellular traps. While some studies propose nuclear DNA release due to cell death in eosinophils in a process termed EETosis,[39] our work emphasizes the regulatory impact of mtDNA on MBP-1's toxicity, underscoring its significance within EETs. Moreover, we uncovered a link between CpG DNA methylation levels and the modulation of MBP-1, shedding light on a

distinctive regulatory mechanism. However, further research is required to fully understand the interaction between non-methylated DNA and MBP-1. Additionally, our investigations pinpoint the plasma membrane as the main target of MBP-1, elucidating a rapid cell death process involving plasma membrane permeabilization through the formation of small pores, followed by the loss of membrane integrity as well as efflux of potassium. Last, we highlight the pivotal role of heparin in the regulation of MBP-1 toxicity, achieving a dual outcome of reducing host damage and promoting the bactericidal effect of MBP-1, which presents a promising approach for therapeutic applications.

Limitations of the study

Our study has certain limitations. The key observations were made using the MBP-1-derived peptide MBP-$1_{18–45}$. This approach was necessary due to unsuccessful attempts to synthesize the full-length protein via a bacterial expression system, attributed to the potent antibacterial characteristics of MBP-1. Nevertheless, the MBP-$1_{18–45}$ peptide retains the aggregation propensities as well as the characteristic antibacterial and cytotoxic properties of the full-length protein, as demonstrated previously.[20] Hence, employing the peptide serves as a reliable tool to investigate the toxic potential of the full-length protein. In addition, the investigation of the functional characteristics of MBP-1 pores in our study is limited to the use of a single membrane model system: GUVs. Although GUVs provide valuable insights into the initial behaviors of MBP-1 pores, a comprehensive understanding and characterization of their functional properties requires the employment of additional biophysical assays.

STAR★METHODS

Detailed methods are provided in the online version of this paper and include the following:

- KEY RESOURCES TABLE
- RESOURCE AVAILABILITY
  - Lead contact
  - Materials availability
  - Data and code availability
- EXPERIMENTAL MODEL AND STUDY PARTICIPANT DETAILS
  - Cell lines and cell culture
  - Mouse
- METHOD DETAILS
  - MBP-1_{18-45} and MBP-1^{*}_{18-45} peptides
  - Bacteria killing assay
  - Cell viability assay
  - DNA isolation
  - Human genomic DNA isolation
  - DNA purification
  - Isolation of mouse eosinophils from peripheral blood
  - Co-culture of mouse eosinophils and BEAS-2B cells
  - DNA methylation quantification
  - Cell death staining
  - Transepithelial electrical resistance (TEER)
  - Scanning electron microscopy
  - Transmission electron microscopy
  - Liposome leakage assay
  - Giant unilamellar vesicle (GUV)
  - GUV imaging
  - Cryo-electron microscopy
  - Potassium concentration measurement
  - Calcium staining
- QUANTIFICATION AND STATISTICAL ANALYSIS

SUPPLEMENTAL INFORMATION

Supplemental information can be found online at https://doi.org/10.1016/j.celrep.2024.114084.

ACKNOWLEDGMENTS

We thank Meike Claus for technical support and Dr. B. Jack from New England Biolabs for the kind gift of the *M. SssI* plasmid. L.G. and P.M. are PhD students at the Graduate School of Cellular and Biomedical Sciences of the University of Bern. M.B. is a master's student in the Pharmacy program at the University of Ljubljana. G.G. is a master's student in the Laboratory Biomedicine program at the University of Ljubljana. Microscopy images and electron microscopy sample preparation were performed with devices supported by the Microscopy Imaging Center (MIC) of the University of Bern, Switzerland. This work was supported by the Swiss National Science Foundation, Switzerland (grant 31003A_179520 to B.Z., grant 31003A_173215 to S.Y., and grant 310030_184816 to H.-U.S.).

AUTHOR CONTRIBUTIONS

Conceptualization, S.Y. and H.-U.S.; formal analysis, L.G., P.M., and S.Y.; funding acquisition, B.Z., S.Y., and H.-U.S.; investigation, L.G., P.M., B.H., I.I., M.B., G.G., and S.Y.; methodology, L.G., P.M., B.H., I.I., C.v.B., B.Z., A.S., and S.Y.; project administration, S.Y. and H.-U.S.; resources, C.v.B., B.Z., S.Y., and H.-U.S.; software, C.v.B., B.Z., and S.Y.; supervision, S.Y. and H.-U.S.; writing – original draft, L.G. and S.Y.; writing – review and editing, P.M., C.v.B., A.S., B.Z., S.Y., and H.-U.S. All authors have read and agreed to the published version of the manuscript.

DECLARATION OF INTERESTS

The authors declare no competing interests.

Received: October 6, 2023
Revised: December 28, 2023
Accepted: March 25, 2024

REFERENCES

1. Geering, B., Stoeckle, C., Conus, S., and Simon, H.U. (2013). Living and dying for inflammation: neutrophils, eosinophils, basophils. Trends Immunol. *34*, 398–409. https://doi.org/10.1016/j.it.2013.04.002.
2. Radonjic-Hösli, S., and Simon, H.U. (2014). Eosinophils. Chem. Immunol. Allergy *100*, 193–204. https://doi.org/10.1159/000358735.
3. Ramirez, G.A., Yacoub, M.R., Ripa, M., Mannina, D., Cariddi, A., Saporiti, N., Ciceri, F., Castagna, A., Colombo, G., and Dagna, L. (2018). Eosinophils from physiology to disease: a comprehensive review. BioMed Res. Int. *2018*, 9095275. https://doi.org/10.1155/2018/9095275.
4. O'Flaherty, S.M., Sutummaporn, K., Häggtoft, W.L., Worrall, A.P., Rizzo, M., Braniste, V., Höglund, P., Kadri, N., and Chambers, B.J. (2017). TLR-stimulated eosinophils mediate recruitment and activation of NK cells in vivo. Scand. J. Immunol. *85*, 417–424. https://doi.org/10.1111/sji.12554.
5. Elishmereni, M., Bachelet, I., Nissim Ben-Efraim, A.H., Mankuta, D., and Levi-Schaffer, F. (2013). Interacting mast cells and eosinophils acquire

an enhanced activation state in vitro. Allergy *68*, 171–179. https://doi.org/10.1111/all.12059.

6. Wong, T.W., Doyle, A.D., Lee, J.J., and Jelinek, D.F. (2014). Eosinophils regulate peripheral B cell numbers in both mice and humans. JJ. Immunol. *192*, 3548–3558. https://doi.org/10.4049/jimmunol.1302241.
7. Chu, V.T., Fröhlich, A., Steinhauser, G., Scheel, T., Roch, T., Fillatreau, S., Lee, J.J., Löhning, M., and Berek, C. (2011). Eosinophils are required for the maintenance of plasma cells in the bone marrow. Nat. Immunol. *12*, 151–159. https://doi.org/10.1038/ni.1981.
8. Chen, H.H., Sun, A.H., Ojcius, D.M., Hu, W.L., Ge, Y.M., Lin, X., Li, L.J., Pan, J.P., and Yan, J. (2015). Eosinophils from murine lamina propria induce differentiation of naive T cells into regulatory T cells via TGF-beta1 and retinoic acid. PLoS One *10*, e0142881. https://doi.org/10.1371/journal.pone.0142881.
9. Gigon, L., Fettrelet, T., Yousefi, S., Simon, D., and Simon, H.U. (2023). Eosinophils from a to z. Allergy *78*, 1810–1846. https://doi.org/10.1111/all.15751.
10. Weller, P.F., and Spencer, L.A. (2017). Functions of tissue-resident eosinophils. Nat. Rev. Immunol. *17*, 746–760. https://doi.org/10.1038/nri.2017.95.
11. Marichal, T., Mesnil, C., and Bureau, F. (2017). Homeostatic eosinophils: characteristics and functions. Front. Med. *4*, 101. https://doi.org/10.3389/fmed.2017.00101.
12. Sugawara, R., Lee, E.J., Jang, M.S., Jeun, E.J., Hong, C.P., Kim, J.H., Park, A., Yun, C.H., Hong, S.W., Kim, Y.M., et al. (2016). Small intestinal eosinophils regulate Th17 cells by producing IL-1 receptor antagonist. JJ. Exp. Med. *213*, 555–567. https://doi.org/10.1084/jem.20141388.
13. Albinsson, S., Lingblom, C., Lundqvist, C., Telemo, E., Ekwall, O., and Wennerås, C. (2021). Eosinophils interact with thymocytes and proliferate in the human thymus. Eur. J. Immunol. *51*, 1539–1541. https://doi.org/10.1002/eji.202049080.
14. Larrick, J.W., and Mendelsohn, A.R. (2020). Eosinophils and white fat: protection from worms and inflammaging. Rejuvenation Res. *23*, 349–352. https://doi.org/10.1089/rej.2020.2375.
15. Simon, H.U., Yousefi, S., Germic, N., Arnold, I.C., Haczku, A., Karaulov, A.V., Simon, D., and Rosenberg, H.F. (2020). The cellular functions of eosinophils: Collegium Internationale Allergologicum (CIA) Update 2020. Int. Arch. Allergy Immunol. *181*, 11–23. https://doi.org/10.1159/000504847.
16. Coden, M.E., and Berdnikovs, S. (2020). Eosinophils in wound healing and epithelial remodeling: Is coagulation a missing link? J. Leukoc. Biol. *108*, 93–103. https://doi.org/10.1002/JLB.3MR0120-390R.
17. DeNichilo, M.O., Shoubridge, A.J., Panagopoulos, V., Liapis, V., Zysk, A., Zinonos, I., Hay, S., Atkins, G.J., Findlay, D.M., and Evdokiou, A. (2016). Peroxidase enzymes regulate collagen biosynthesis and matrix mineralization by cultured human osteoblasts. Calcif. Tissue Int. *98*, 294–305. https://doi.org/10.1007/s00223-015-0090-6.
18. Melo, R.C.N., and Weller, P.F. (2018). Contemporary understanding of the secretory granules in human eosinophils. J. Leukoc. Biol. *104*, 85–93. https://doi.org/10.1002/JLB.3MR1217-476R.
19. Yousefi, S., Gold, J.A., Andina, N., Lee, J.J., Kelly, A.M., Kozlowski, E., Schmid, I., Straumann, A., Reichenbach, J., Gleich, G.J., and Simon, H.U. (2008). Catapult-like release of mitochondrial DNA by eosinophils contributes to antibacterial defense. Nat. Med. *14*, 949–953. https://doi.org/10.1038/nm.1855.
20. Soragni, A., Yousefi, S., Stoeckle, C., Soriaga, A.B., Sawaya, M.R., Kozlowski, E., Schmid, I., Radonjic-Hoesli, S., Boutet, S., Williams, G.J., et al. (2015). Toxicity of eosinophil MBP is repressed by intracellular crystallization and promoted by extracellular aggregation. Mol. Cell *57*, 1011–1021. https://doi.org/10.1016/j.molcel.2015.01.026.
21. Akuthota, P., Wang, H.B., Spencer, L.A., and Weller, P.F. (2008). Immunoregulatory roles of eosinophils: a new look at a familiar cell. Clin. Exp. Allergy *38*, 1254–1263. https://doi.org/10.1111/j.1365-2222.2008.03037.x.
22. Lehrer, R.I., Szklarek, D., Barton, A., Ganz, T., Hamann, K.J., and Gleich, G.J. (1989). Antibacterial properties of eosinophil major basic protein and eosinophil cationic protein. JJ. Immunol. *142*, 4428–4434.
23. Acharya, K.R., and Ackerman, S.J. (2014). Eosinophil granule proteins: form and function. J. Biol. Chem. *289*, 17406–17415. https://doi.org/10.1074/jbc.R113.546218.
24. Wright, B.L., Leiferman, K.M., and Gleich, G.J. (2011). Eosinophil granule protein localization in eosinophilic endomyocardial disease. N. Engl. J. Med. *365*, 187–188. https://doi.org/10.1056/NEJMc1103005.
25. Peters, M.S., Schroeter, A.L., and Gleich, G.J. (1983). Immunofluorescence identification of eosinophil granule major basic protein in the flame figures of Wells' syndrome. Br. J. Dermatol. *109*, 141–148. https://doi.org/10.1111/j.1365-2133.1983.tb07074.x.
26. Leiferman, K.M., Ackerman, S.J., Sampson, H.A., Haugen, H.S., Venencie, P.Y., and Gleich, G.J. (1985). Dermal deposition of eosinophil-granule major basic protein in atopic dermatitis. Comparison with onchocerciasis. N. Engl. J. Med. *313*, 282–285. https://doi.org/10.1056/NEJM198508013130502.
27. Brinkmann, V., Reichard, U., Goosmann, C., Fauler, B., Uhlemann, Y., Weiss, D.S., Weinrauch, Y., and Zychlinsky, A. (2004). Neutrophil extracellular traps kill bacteria. Science *303*, 1532–1535. https://doi.org/10.1126/science.1092385.
28. Morshed, M., Hlushchuk, R., Simon, D., Walls, A.F., Obata-Ninomiya, K., Karasuyama, H., Djonov, V., Eggel, A., Kaufmann, T., Simon, H.U., and Yousefi, S. (2014). NADPH oxidase-independent formation of extracellular DNA traps by basophils. JJ. Immunol. *192*, 5314–5323. https://doi.org/10.4049/jimmunol.1303418.
29. von Kockritz-Blickwede, M., Goldmann, O., Thulin, P., Heinemann, K., Norrby-Teglund, A., Rohde, M., and Medina, E. (2008). Phagocytosis-independent antimicrobial activity of mast cells by means of extracellular trap formation. Blood *111*, 3070–3080. https://doi.org/10.1182/blood-2007-07-104018.
30. Yousefi, S., Morshed, M., Amini, P., Stojkov, D., Simon, D., von Gunten, S., Kaufmann, T., and Simon, H.U. (2015). Basophils exhibit antibacterial activity through extracellular trap formation. Allergy *70*, 1184–1188. https://doi.org/10.1111/all.12662.
31. Fettrelet, T., Gigon, L., Karaulov, A., Yousefi, S., and Simon, H.U. (2021). The enigma of eosinophil degranulation. Int. J. Mol. Sci. *22*, 7091. https://doi.org/10.3390/ijms22137091.
32. Klopf, J., Brostjan, C., Eilenberg, W., and Neumayer, C. (2021). Neutrophil extracellular traps and their implications in cardiovascular and inflammatory disease. Int. J. Mol. Sci. *22*, 559. https://doi.org/10.3390/ijms22020559.
33. Simon, D., Simon, H.U., and Yousefi, S. (2013). Extracellular DNA traps in allergic, infectious, and autoimmune diseases. Allergy *68*, 409–416. https://doi.org/10.1111/all.12111.
34. Yousefi, S., Simon, D., and Simon, H.U. (2012). Eosinophil extracellular DNA traps: molecular mechanisms and potential roles in disease. Curr. Opin. Immunol. *24*, 736–739. https://doi.org/10.1016/j.coi.2012.08.010.
35. Germic, N., Stojkov, D., Oberson, K., Yousefi, S., and Simon, H.U. (2017). Neither eosinophils nor neutrophils require ATG5-dependent autophagy for extracellular DNA trap formation. Immunology *152*, 517–525. https://doi.org/10.1111/imm.12790.
36. Amini, P., Stojkov, D., Felser, A., Jackson, C.B., Courage, C., Schaller, A., Gelman, L., Soriano, M.E., Nuoffer, J.M., Scorrano, L., et al. (2018). Neutrophil extracellular trap formation requires OPA1-dependent glycolytic ATP production. Nat. Commun. *9*, 2958. https://doi.org/10.1038/s41467-018-05387-y.
37. Gigon, L., Fettrelet, T., Miholic, M., McLeish, K.R., Yousefi, S., Stojkov, D., and Simon, H.U. (2023). Syntaxin-4 and SNAP23 are involved in neutrophil degranulation, but not in the release of mitochondrial DNA during NET formation. Front. Immunol. *14*, 1272699. https://doi.org/10.3389/fimmu.2023.1272699.

38. Yousefi, S., Stojkov, D., Germic, N., Simon, D., Wang, X., Benarafa, C., and Simon, H.U. (2019). Untangling "NETosis" from NETs. Eur. J. Immunol. *49*, 221–227. https://doi.org/10.1002/eji.201747053.

39. Ueki, S., Melo, R.C.N., Ghiran, I., Spencer, L.A., Dvorak, A.M., and Weller, P.F. (2013). Eosinophil extracellular DNA trap cell death mediates lytic release of free secretion-competent eosinophil granules in humans. Blood *121*, 2074–2083. https://doi.org/10.1182/blood-2012-05-432088.

40. Muniz, V.S., Silva, J.C., Braga, Y.A.V., Melo, R.C.N., Ueki, S., Takeda, M., Hebisawa, A., Asano, K., Figueiredo, R.T., and Neves, J.S. (2018). Eosinophils release extracellular DNA traps in response to Aspergillus fumigatus. J. Allergy Clin. Immunol. *141*, 571–585.e7. https://doi.org/10.1016/j.jaci.2017.07.048.

41. Gleich, G.J., Frigas, E., Loegering, D.A., Wassom, D.L., and Steinmuller, D. (1979). Cytotoxic properties of the eosinophil major basic protein. JJ. Immunol. *123*, 2925–2927.

42. Tetz, G., and Tetz, V. (2021). Bacterial extracellular DNA promotes beta-Amyloid aggregation. Microorganisms *9*, 1301. https://doi.org/10.3390/microorganisms9061301.

43. Zhang, Q., Raoof, M., Chen, Y., Sumi, Y., Sursal, T., Junger, W., Brohi, K., Itagaki, K., and Hauser, C.J. (2010). Circulating mitochondrial DAMPs cause inflammatory responses to injury. Nature *464*, 104–107. https://doi.org/10.1038/nature08780.

44. Yousefi, S., Mihalache, C., Kozlowski, E., Schmid, I., and Simon, H.U. (2009). Viable neutrophils release mitochondrial DNA to form neutrophil extracellular traps. Cell Death Differ. *16*, 1438–1444. https://doi.org/10.1038/cdd.2009.96.

45. Germic, N., Fettrelet, T., Stojkov, D., Hosseini, A., Horn, M.P., Karaulov, A., Simon, D., Yousefi, S., and Simon, H.U. (2021). The release kinetics of eosinophil peroxidase and mitochondrial DNA is different in association with eosinophil extracellular trap formation. Cells *10*, 306. https://doi.org/10.3390/cells10020306.

46. Casadesús, J., and Low, D. (2006). Epigenetic gene regulation in the bacterial world. Microbiol. Mol. Biol. Rev. *70*, 830–856. https://doi.org/10.1128/MMBR.00016-06.

47. Guitton, R., Nido, G.S., and Tzoulis, C. (2022). No evidence of extensive non-CpG methylation in mtDNA. Nucleic Acids Res. *50*, 9190–9194. https://doi.org/10.1093/nar/gkac701.

48. Martín-Sánchez, F., Diamond, C., Zeitler, M., Gomez, A.I., Baroja-Mazo, A., Bagnall, J., Spiller, D., White, M., Daniels, M.J.D., Mortellaro, A., et al. (2016). Inflammasome-dependent IL-1beta release depends upon membrane permeabilisation. Cell Death Differ. *23*, 1219–1231. https://doi.org/10.1038/cdd.2015.176.

49. Borges, J.P., Sætra, R.S.R., Volchuk, A., Bugge, M., Devant, P., Sporsheim, B., Kilburn, B.R., Evavold, C.L., Kagan, J.C., Goldenberg, N.M., et al. (2022). Glycine inhibits NINJ1 membrane clustering to suppress plasma membrane rupture in cell death. Elife *11*, e78609. https://doi.org/10.7554/eLife.78609.

50. Dal Peraro, M., and van der Goot, F.G. (2016). Pore-forming toxins: ancient, but never really out of fashion. Nat. Rev. Microbiol. *14*, 77–92. https://doi.org/10.1038/nrmicro.2015.3.

51. Zhang, Y., Chen, X., Gueydan, C., and Han, J. (2018). Plasma membrane changes during programmed cell deaths. Cell Res. *28*, 9–21. https://doi.org/10.1038/cr.2017.133.

52. Walev, I., Palmer, M., Valeva, A., Weller, U., and Bhakdi, S. (1995). Binding, oligomerization, and pore formation by streptolysin O in erythrocytes and fibroblast membranes: detection of nonlytic polymers. Infect. Immun. *63*, 1188–1194. https://doi.org/10.1128/iai.63.4.1188-1194.1995.

53. Bruggisser, J., Tarek, B., Wyder, M., Müller, P., von Ballmoos, C., Witz, G., Enzmann, G., Deutsch, U., Engelhardt, B., and Posthaus, H. (2020). CD31 (PECAM-1) serves as the endothelial cell-specific receptor of Clostridium perfringens beta-Toxin. Cell Host Microbe *28*, 69–78.e6. https://doi.org/10.1016/j.chom.2020.05.003.

54. Fringeli, U.P., and Fringeli, M. (1979). Pore formation in lipid membranes by alamethicin. Proc. Natl. Acad. Sci. USA *76*, 3852–3856. https://doi.org/10.1073/pnas.76.8.3852.

55. Mondal, A.K., Lata, K., Singh, M., Chatterjee, S., Chauhan, A., Puravankara, S., and Chattopadhyay, K. (2022). Cryo-EM elucidates mechanism of action of bacterial pore-forming toxins. Biochim. Biophys. Acta. Biomembr. *1864*, 184013. https://doi.org/10.1016/j.bbamem.2022.184013.

56. Scott, H., Huang, W., Bann, J.G., and Taylor, D.J. (2018). Advances in structure determination by cryo-EM to unravel membrane-spanning pore formation. Protein Sci. *27*, 1544–1556. https://doi.org/10.1002/pro.3454.

57. Kleine, T.J., Gleich, G.J., and Lewis, S.A. (1998). Eosinophil major basic protein increases membrane permeability in mammalian urinary bladder epithelium. Am. J. Physiol. *275*, C93–C103. https://doi.org/10.1152/ajpcell.1998.275.1.C93.

58. Pinkwart, K., Schneider, F., Lukoseviciute, M., Sauka-Spengler, T., Lyman, E., Eggeling, C., and Sezgin, E. (2019). Nanoscale dynamics of cholesterol in the cell membrane. J. Biol. Chem. *294*, 12599–12609. https://doi.org/10.1074/jbc.RA119.009683.

59. Di Scala, C., Yahi, N., Boutemeur, S., Flores, A., Rodriguez, L., Chahinian, H., and Fantini, J. (2016). Common molecular mechanism of amyloid pore formation by Alzheimer's beta-amyloid peptide and alpha-synuclein. Sci. Rep. *6*, 28781. https://doi.org/10.1038/srep28781.

60. Tweten, R.K., Hotze, E.M., and Wade, K.R. (2015). The unique molecular choreography of giant pore formation by the cholesterol-dependent cytolysins of gram-positive bacteria. Annu. Rev. Microbiol. *69*, 323–340. https://doi.org/10.1146/annurev-micro-091014-104233.

61. Johnstone, B.A., Joseph, R., Christie, M.P., Morton, C.J., McGuiness, C., Walsh, J.C., Böcking, T., Tweten, R.K., and Parker, M.W. (2022). Cholesterol-dependent cytolysins: The outstanding questions. IUBMB Life *74*, 1169–1179. https://doi.org/10.1002/iub.2661.

62. Sierig, G., Cywes, C., Wessels, M.R., and Ashbaugh, C.D. (2003). Cytotoxic effects of streptolysin o and streptolysin s enhance the virulence of poorly encapsulated group a streptococci. Infect. Immun. *71*, 446–455. https://doi.org/10.1128/IAI.71.1.446-455.2003.

63. Palmer, M., Harris, R., Freytag, C., Kehoe, M., Tranum-Jensen, J., and Bhakdi, S. (1998). Assembly mechanism of the oligomeric streptolysin O pore: the early membrane lesion is lined by a free edge of the lipid membrane and is extended gradually during oligomerization. EMBO J. *17*, 1598–1605. https://doi.org/10.1093/emboj/17.6.1598.

64. Kreiser, R.P., Wright, A.K., Sasser, L.R., Rinauro, D.J., Gabriel, J.M., Hsu, C.M., Hurtado, J.A., McKenzie, T.L., Errico, S., Albright, J.A., et al. (2022). A brain-permeable aminosterol regulates cell membranes to mitigate the toxicity of diverse pore-forming agents. ACS Chem. Neurosci. *13*, 1219–1231. https://doi.org/10.1021/acschemneuro.1c00840.

65. Li, Y., Li, Y., Mengist, H.M., Shi, C., Zhang, C., Wang, B., Li, T., Huang, Y., Xu, Y., and Jin, T. (2021). Structural basis of the pore-forming toxin/membrane interaction. Toxins *13*, 128. https://doi.org/10.3390/toxins13020128.

66. Yilmaz, N., Yamaji-Hasegawa, A., Hullin-Matsuda, F., and Kobayashi, T. (2018). Molecular mechanisms of action of sphingomyelin-specific pore-forming toxin, lysenin. Semin. Cell Dev. Biol. *73*, 188–198. https://doi.org/10.1016/j.semcdb.2017.07.036.

67. Morgan, A.J., and Jacob, R. (1994). Ionomycin enhances Ca2+ influx by stimulating store-regulated cation entry and not by a direct action at the plasma membrane. Biochem. J. *300*, 665–672. https://doi.org/10.1042/bj3000665.

68. Milanesi, L., Sheynis, T., Xue, W.F., Orlova, E.V., Hellewell, A.L., Jelinek, R., Hewitt, E.W., Radford, S.E., and Saibil, H.R. (2012). Direct three-dimensional visualization of membrane disruption by amyloid fibrils. Proc Natl Acad Sci USA *109*, 20455–20460. https://doi.org/10.1073/pnas.1206325109.

69. Flores-Romero, H., Ros, U., and Garcia-Saez, A.J. (2020). Pore formation in regulated cell death. EMBO J. *39*, e105753. https://doi.org/10.15252/embj.2020105753.

70. Last, N.B., and Miranker, A.D. (2013). Common mechanism unites membrane poration by amyloid and antimicrobial peptides. Proc Natl Acad Sci USA *110*, 6382–6387. https://doi.org/10.1073/pnas.1219059110.

71. McCarthy, J.V., and Cotter, T.G. (1997). Cell shrinkage and apoptosis: a role for potassium and sodium ion efflux. Cell Death Differ. *4*, 756–770. https://doi.org/10.1038/sj.cdd.4400296.

72. Bachmann, M., Li, W., Edwards, M.J., Ahmad, S.A., Patel, S., Szabo, I., and Gulbins, E. (2020). Voltage-gated potassium channels as regulators of cell death. Front. Cell Dev. Biol. *8*, 611853. https://doi.org/10.3389/fcell.2020.611853.

73. Cheng, C.J., Kuo, E., and Huang, C.L. (2013). Extracellular potassium homeostasis: insights from hypokalemic periodic paralysis. Semin. Nephrol. *33*, 237–247. https://doi.org/10.1016/j.semnephrol.2013.04.004.

74. Butterfield, S.M., and Lashuel, H.A. (2010). Amyloidogenic protein-membrane interactions: mechanistic insight from model systems. Angew. Chem. Int. Ed. Engl. *49*, 5628–5654. https://doi.org/10.1002/anie.200906670.

75. Tetz, G., Pinho, M., Pritzkow, S., Mendez, N., Soto, C., and Tetz, V. (2020). Bacterial DNA promotes Tau aggregation. Sci. Rep. *10*, 2369. https://doi.org/10.1038/s41598-020-59364-x.

76. Yousefi, S., Simon, D., Stojkov, D., Karsonova, A., Karaulov, A., and Simon, H.U. (2020). In vivo evidence for extracellular DNA trap formation. Cell Death Dis. *11*, 300. https://doi.org/10.1038/s41419-020-2497-x.

77. Germic, N., Hosseini, A., Stojkov, D., Oberson, K., Claus, M., Benarafa, C., Calzavarini, S., Angelillo-Scherrer, A., Arnold, I.C., Muller, A., et al. (2021). ATG5 promotes eosinopoiesis but inhibits eosinophil effector functions. Blood *137*, 2958–2969. https://doi.org/10.1182/blood.2020010208.

78. Fletcher, B.S. (2008). Development and validation of an approach to produce large-scale quantities of CpG-methylated plasmid DNA. Microb. Biotechnol. *1*, 62–67. https://doi.org/10.1111/j.1751-7915.2007.00007.x.

79. Ślaska-Kiss, K., Zsibrita, N., Koncz, M., Albert, P., Csábrádi, Á., Szentes, S., and Kiss, A. (2021). Lowering DNA binding affinity of SssI DNA methyltransferase does not enhance the specificity of targeted DNA methylation in E. coli. Sci. Rep. *11*, 15226. https://doi.org/10.1038/s41598-021-94528-3.

80. Zindel, J., Peiseler, M., Hossain, M., Deppermann, C., Lee, W.Y., Haenni, B., Zuber, B., Deniset, J.F., Surewaard, B.G.J., Candinas, D., and Kubes, P. (2021). Primordial GATA6 macrophages function as extravascular platelets in sterile injury. Science *371*, eabe0595. https://doi.org/10.1126/science.abe0595.

81. Dolder, N., Müller, P., and von Ballmoos, C. (2022). Experimental platform for the functional investigation of membrane proteins in giant unilamellar vesicles. Soft Matter *18*, 5877–5893. https://doi.org/10.1039/d2sm00551d.

STAR★METHODS

KEY RESOURCES TABLE

REAGENT or RESOURCE	SOURCE	IDENTIFIER
Antibodies		
Capture Antibody	Sigma-Aldrich	Cat#C3493
Detection Antibody	Sigma-Aldrich	Cat#D8818
Bacterial and virus strains		
Escherichia coli: M91655-GFP	E. Slack, ETH Zurich, Zurich, CH	N/A
Escherichia coli: K12 ER18121	New England Biolabs, Ipswich, MA, USA	E4102
Chemicals, peptides, and recombinant proteins		
MBP-1_{18-45}	ThermoFisher Scientific	Custom-synthesized; Sequence: FTCRRCYRGN LVSIHNFNIN YRIQCSVS
MBP-1^{*}_{18-45}	ThermoFisher Scientific	Custom-synthesized; Sequence: FTCRRCYRGN PVSIHPFNIN YRPQCSVS
Heparin ammonium salt from porcine intestinal mucosa	Sigma-Aldrich	Cat#H6279
Propidium iodide	Molecular Probes	Cat#P3566
Punicalagin	Sigma-Aldrich	Cat#P0023
Glycine	Sigma-Aldrich	Cat#G8790
Streptolysin O from *Streptococcus pyogenes*	Sigma-Aldrich	Cat#S0149
5-aza-2′-deoxycytidine	Sigma-Aldrich	Cat#A3656
Histopaque 1119	Sigma-Aldrich	Cat#1119-1
CellTracker™ Deep Red	ThermoFisher Scientific	Cat#C34565
Hoechst 33342	Molecular Probes	Cat#H3570
MitoSOX™ Mitochondrial Superoxide Indicators	ThermoFisher Scientific	Cat#M36008
Recombinant Mouse GM-CSF protein	R&D Systems	Cat#415-ML
C5a, Mouse, Recombinant	Hycult Biotech	Cat#HC1101
Soy Extract Polar	Avanti Polar Lipids	Cat#541602
Liver Extract Total	Avanti Polar Lipids	Cat#181104
Cholesterol	Avanti Polar Lipids	Cat#700000
Sphingomyelin	Sigma-Aldrich	Cat#S0756
DSPE-PEG(2000) Biotin	Avanti Polar Lipids	Cat#880129
5(6)-carboxyfluorescein	Sigma-Aldrich	Cat#21877
18:1 Liss Rhod PE	Avanti Polar Lipids	Cat#810150
Oregon Green™ 488 DHPE	Invitrogen	Cat#O12650
8-Hydroxypyrene-1,3,6-trisulfonic acid trisodium salt	Invitrogen	Cat#H348
Dextran, Texas Red™, 3000 MW, neutral	Invitrogen	Cat#D3329
Dextran, Texas Red™, 10,000 MW, Lysine Fixable	Invitrogen	Cat#D1863
Alamethicin	Sigma-Aldrich	Cat#A4665
Methyl-β-cyclodextrin	Sigma-Aldrich	Cat#C4555
Claramine trifluoroacetate salt	Sigma-Aldrich	Cat#SML1545
Sphingomyelinase from *Staphylococcus aureus*	Sigma-Aldrich	Cat#S8633
IPG-1 AM	Ion Biosciences	Cat#3041F
Fluo-3 AM	Enzo	Cat#ENZ.52004

(*Continued on next page*)

Continued

REAGENT or RESOURCE	SOURCE	IDENTIFIER
Ionomycin calcium	LKT Laboratories	Cat#I5753
Pharmacological inhibitors	Table S1	Table S1
Critical commercial assays		
Imprint® Methylated DNA Quantification Kit	Sigma-Aldrich	Cat#MDQ1
EasySep Mouse PE Positive Selection Kit	StemCell Technologies	Cat#18554
LIVE/DEAD™ Viability/Cytotoxicity Kit	Invitrogen	Cat#L3224
Experimental models: Cell lines		
Human: BEAS-2B cells	A. Gazhar, University of Bern, Bern, CH	N/A
Human: HL-60 cells	ATCC	CRL-1964
Experimental models: Organisms/strains		
Mouse: B6; 129-Gt(ROSA)26Sortm4 (CAG-EGFP*)Nat	The Jackson Laboratory	Strain Code: 021429
Mouse: Tg(Cd3d-Il5)NJ.1638Nal	J.J. Lee, Mayo Clinic, Scottsdale, AZ, USA	N/A
Recombinant DNA		
Plasmid: M. SssI	B. Jack, New England Biolabs	N/A
Software and algorithms		
FlowJo 10.6	Treestar	N/A
Imaris 10.0.1	Oxford Instruments	N/A
Prism 8.0	GraphPad	N/A

RESOURCE AVAILABILITY

Lead contact

Further information and requests for resources and reagents should be directed to and will be fulfilled by the lead contact, Hans-Uwe Simon (hans-uwe.simon@unibe.ch).

Materials availability

This study did not generate new unique reagents.

Data and code availability

- All data reported in this paper will be shared by the lead contact upon request.
- This paper does not report original code.
- Any additional information required to reanalyze the data reported in this work paper is available from the lead contact upon request.

EXPERIMENTAL MODEL AND STUDY PARTICIPANT DETAILS

Cell lines and cell culture

The human bronchial epithelial cell line BEAS-2B (kindly provided by Dr. Amiq Gazdhar, University of Bern) was cultured in DMEM complemented with 5% FCS at 37°C in 5% CO_2. The promyelocytic cell line derived from a human leukemia cell line HL-60 was purchased from ATCC (Manassas, VA, USA) and maintained in RPMI-1640 with 10% FCS at 37°C in 5% CO_2.

Mouse

Commercially available mito_GFP (021429) were purchased from The Jackson Laboratory. *Il5*^{tg} mice[35,45,77] were intercrossed with mito_GFP mice. All mice were bred and housed at the Central Animal Facility of the University of Bern. Mice were housed in specific pathogen-free facilities in individually ventilated cages (Tecniplast, Green Line, Buguggiate, Italy) within a temperature- and humidity-controlled room, following a 12 h light/12 h dark cycle. The housing temperature for the mice ranged between 20°C and 22°C. Autoclaved acidified water and cages, as well as food, bedding, and environmental enrichment were provided. Mouse eosinophils were isolated from male mice between 6 and 8 weeks of age. The study was approved by the Veterinary Office of the Canton of Bern (license number BE26/2021) and conducted in accordance with Swiss federal legislation on animal welfare.

METHOD DETAILS

MBP-1_{18-45} and MBP-1^*_{18-45} peptides

The sequences of MBP-1_{18-45} and MBP-1^*_{18-45} were adapted from Soragni et al.[20] (MBP-1_{18-45}: FTCRRCYRGN LVSIHNFNIN YRIQCSVS; MBP-1^*_{18-45}: FTCRRCYRGN PVSIHPFNIN YRPQCSVS). Both peptides were synthesized at a purity level of more than 98% (ThermoFisher Scientific, Rockford, IL, USA) and dissolved in 100% DMSO.

Bacteria killing assay

The bacteria killing assay was performed using GFP-labelled *E. coli* M91655 (kindly gifted by E. Slack, ETH Zurich).[20,36] In brief, a single colony of *E. coli*-GFP was cultured overnight in LB medium without antibiotics at 37°C, shaking. The following day, the bacterial culture was diluted 1:100 in LB medium, left grown till mid-logarithmic growth phase, and washed twice with 1x HBSS. Bacteria were gently centrifuged at 100 rcf to removed clumped bacteria and finally diluted to 10^7 cells/mL 1x HBSS.

MBP-1_{18-45} was preincubated with or without DNA and heparin in 1x HBSS for 15 min at room temperature (RT) before mixed at a 1:1 ratio with the same volume of bacteria (final concentration of 0.5 x 10^7 bacterial cells/mL). Bacteria alone were used as negative controls. The samples were incubated for the indicated times at 37°C, shaking. To stop the reaction, an equal amount of ice-cold 1x HBSS was added to each tube and bacteria were put on ice. Bacteria killing was assessed by the loss of the GFP signal using flow cytometry (FACSVerse, BD Biosciences) and analyzed by FlowJo software (Tree Star, Ashland, OR, USA).

Cell viability assay

One day prior to experiments, BEAS-2B cells were trypsinized, seeded at 20′000 cells in a 96-well plate in DMEM supplemented with 5% FCS and allowed to adhere overnight at 37°C.[20] The following day, cells were washed three times with DMEM supplemented with 17 mM HEPES and pretreated with inhibitors at 37 °C at the indicated experiments. MBP-1_{18-45} was preincubated with or without DNA and heparin for 15 min before addition to the cells for the indicated times at RT. At the end of the incubation time, cells were collected by trypsinization. Cell death was assessed by the uptake of PI (10 μg/mL) using flow cytometry (FACSVerse, BD Biosciences) and analyzed by FlowJo software (Tree Star, Ashland, OR, USA).

DNA isolation

Bacterial DNA isolation

E. coli K12 ER18121 bacteria with or without *M. SssI* plasmid (kindly provided by Dr. B. Jack, New England Biolabs, Ipswich, MA, USA) were cultured in LB medium overnight at 37°C, shaking. 50 μg/mL kanamycin was added to the LB medium for selection of the bacteria containing the *M. SssI* plasmid.[78,79] The following day, pelleted bacteria were resuspended in Sucrose/Tris buffer and 0.25 M EDTA in a 2:1 ratio containing freshly added 2 mg/mL lysozyme and incubated for 2 h on ice. Subsequently, 1% SDS and lysis buffer containing 50 mM Tris-HCl pH 8, 62.5 mM EDTA pH 8, and 1% Triton X-100 in ddH_2O were added. The lysates were cleaned using a 10K filter spin column (Sigma-Aldrich) and centrifuged at 5′000 rcf for 10 min. 100 μg/mL RNase A was added to the lysed cells for removal of RNA and the samples were incubated for 1 h at 37°C, shaking.

Mitochondrial DNA isolation

Mitochondrial DNA was isolated from mouse liver due to the substantial mitochondrial content present in liver tissues allowing the extraction of a sufficient quantity of mtDNA. Crucially, the structure, gene arrangement, and minimal CpG DNA methylation levels of mtDNA are highly conserved across mammals, allowing the use of mouse liver tissue as a reliable source of mtDNA in our study. In brief, mouse liver was minced on ice and smashed through a sterile 70-μm mesh nylon cell strainer (Greiner Bio-One, Frickenhausen, Germany) to obtain single cell suspension. The suspension was washed twice with ice-cold PBS and resuspended in mitochondrial isolation buffer containing 200 mM Mannitol, 70 mM Sucrose, 1 mM EDTA and 10 mM HEPES in ddH_2O. Cells were mechanically lysed using a syringe with a 26-gauge needle and subsequently centrifuged twice at 800 rcf for 10 min to remove nuclei, debris, and intact cells. The supernatant was transferred to a new tube and centrifuged at 14′000 rcf for 10 min to collect the mitochondrial fraction. Isolated mitochondria were washed once and resuspended in lysis buffer containing 10 mM Tris-HCl pH 8, 150 mM NaCl and 20 mM EDTA in ddH_2O. 100 μg/mL RNase A was added to the lysed cells for removal of RNA and the samples were incubated for 1 h at 37°C, shaking. Subsequently, 0.2 mg/mL proteinase K and 1% SDS were added, and the lysates were incubated for 1.5 h at 55°C, shaking.

Human genomic DNA isolation

HL-60 cells were cultured in RPMI-1640 medium containing 10% FCS in presence and absence of DNA demethylating agent 5-aza-2′-CdR (0.3 μM) for 4 days. Cells were lysed with lysis buffer containing 50 mM NaCl, 10 mM Tris-HCl pH 8 and 10 mM EDTA pH 8 in ddH_2O. Shortly before use, 1% SDS and 0.2 mg/mL proteinase K were added to the lysis buffer. Cells were lysed for 2 h at 55°C, shaking. The lysates were cleaned using a 10K filter spin column (Sigma-Aldrich) and centrifuged at 5′000 rcf for 10 min. 100 μg/mL RNase A was added to the lysed cells for removal of RNA and the samples were incubated for 1 h at 37°C, shaking.

DNA purification

Isolated DNA was purified by phenol:chloroform purification and recovered after addition of 0.4 M NaCl solution and one volume of isopropanol. After resuspension in ddH_2O, the concentration and purity of DNA was determined by spectrophotometer (ND-1000; NanoDrop Technologies, Wilmington, DE, USA).

Isolation of mouse eosinophils from peripheral blood

Mouse eosinophils were isolated from the peripheral blood of interleukin (IL)-5 transgenic mice (kindly provided by J. J. Lee, Mayo Clinic, Scottsdale, AZ, USA) to increase the number of circulating eosinophils.[77] In brief, blood was collected from the retro-orbital sinus of mice sedated with isoflurane using heparinized disposable glass pipettes. The blood was diluted 1:1 with PBS, carefully layered over Histopaque 1119 (1.119 g/mL density) (Sigma-Aldrich) and centrifuged at 800 rcf for 20 min. The interface containing eosinophils was collected, treated with ice-cold ddH_2O for 30 s to lyse erythrocytes followed by a washing step with PBS. Subsequently, cells were resuspended to 1 x 10^8 cells/mL in PBS supplemented with 2% FCS and eosinophils were isolated using an EasySep Mouse PE Positive Selection Kit (Stemcell Technologies, Köln, Germany) according to manufacturer's instructions. The purity of isolated eosinophils (>90%) was assessed by Hemacolor Rapid Staining and light microscopic analysis.

Co-culture of mouse eosinophils and BEAS-2B cells

One day prior to the experiments, BEAS-2B cells were trypsinized, seeded at 50′000 cells in a black, glass bottom 24-well plate (Greiner Bio-One) in DMEM supplemented with 5% FCS, and allowed to adhere overnight at 37°C. The following day, cells were washed three times with DMEM supplemented with 17 mM and stained with 0.1 μM CellTracker Deep Red and 1 μg/mL Hoechst 33342 for 30 min at 37°C. Cells were washed twice with PBS and twice with DMEM supplemented with 17 mM HEPES.

Freshly isolated mouse eosinophils were prepared to 0.25 x 10^6 cells in 250 μL in X-VIVO 15 medium, stained with 5 μM MitoSOX and 1 μg/mL Hoechst 33342, primed with 25 ng/mL GM-CSF and incubated with BEAS-2B cells for 20 min at 37°C. At the end of incubation time, eosinophils were activated with 10 nM C5a, and images were collected after 50 min of co-culture of mouse eosinophils and BEAS-2B cells by confocal laser scanning microscopy (LSM 800 with airyscan, Carl Zeiss Micro Imaging GmbH, Jena, Germany) using a Plan-Apochromat 40x/1.4 Oil DIC objective. Single images were analyzed using Imaris software (Bitplane AG, Zurich, Switzerland). For better visualization, min/max thresholds, and gamma correction of Imaris software were used to optimize the image display.[45]

DNA methylation quantification

DNA methylation levels were evaluated using the Imprint Methylated DNA Quantification Kit (Sigma-Aldrich) according to the manufacturer's protocol. In brief, 100 ng of sample or control DNA was diluted in DNA binding solution, added in duplicates to the pretreated 96-well plate and incubated for 1 h at 37°C. Wells were blocked with blocking solution for 30 min at 37°C and subsequently washed three times with wash buffer. Capture antibody (provided in the kit) was added to the wells and incubated for 1 h at RT. Following four washes with wash buffer, detection antibody (provided in the kit) was added and incubated for 30 min at RT. Wells were washed five times with wash buffer and developing solution was added. After an incubation time of 1–10 min at RT, the solution turned blue and stop solution was added causing the reaction mixture to change color to yellow. Relative DNA methylation levels were assessed by absorbance at 450 nm using a SpectraMax M2 plate reader (Molecular Devices, Biberach an der Riss, Germany).

Cell death staining

One day prior to the experiments, BEAS-2B cells were trypsinized, seeded at 100′000 cells in a black, glass-bottom 24-well plate (Greiner Bio-One) in DMEM supplemented with 5% FCS, and allowed to adhere overnight at 37°C. The following day, cells were washed three times with DMEM supplemented with 17 mM HEPES and stained with 4 μM Ethidium Homodimer-1, 0.2 μM calcein AM, and 1 μg/mL Hoechst 33342 for 30 min at 37°C. Cells were treated with MBP-1_{18-45} and images were acquired in live cell microscopy experiments by confocal laser scanning microscopy (LSM 800, Carl Zeiss Micro Imaging GmbH, Jena, Germany) using a Plan-Apochromat 40x/1.4 Oil DIC objective. Images were analyzed using Imaris software (Bitplane AG, Zurich, Switzerland).

Transepithelial electrical resistance (TEER)

One day prior to the experiments, BEAS-2B cells were trypsinized, seeded at 50′000 cells on 8.0 μm pore polycarbonate membrane inserts in a 6.5 mm Transwell (Corning, New York, USA) in DMEM supplemented with 5% FCS, and allowed to adhere overnight at 37°C. The following day, cells were washed three times with DMEM supplemented with 17 mM HEPES and pretreated with or without 50 μM punicalagin for 30 min at 37°C. MBP-1_{18-45} was preincubated with or without DNA and heparin for 15 min at RT before addition to the cells. TEER was measured using a Millicell ERS-2 V-Ohm Meter (Merck KGaA, Darmstadt, Germany) and was calculated as follows: (resistance of treated cells – resistance of blank well) normalized to untreated cells.

Scanning electron microscopy

One day prior to the experiments, BEAS-2B cells were trypsinized, seeded at 200′000 cells on 18 × 18 mm glass in DMEM supplemented with 5% FCS, and allowed to adhere overnight at 37°C. The following day, cells were washed three times with DMEM supplemented with 17 mM HEPES and pretreated with inhibitors for 30 min at 37°C in 5% CO_2 at the indicated experiments. MBP-1_{18-45}

was preincubated with or without DNA and heparin for 15 min before addition to the cells for the indicated times at RT. At the end of the incubation time, cells were fixed in 2.5% glutaraldehyde in 0.15 M HEPES with an osmolarity of 665 and a pH adjusted to 7.39 for at least 24 h before further processed. Samples were then washed three times with 0.15 M HEPES for 5 min, postfixed with 1% OsO_4 in 0.1 M Na-Cacodylate-buffer for 1 h at 4°C. Thereafter, cells were washed three times in 0.1 M Na-Cacodylate-buffer for 5 min and dehydrated in 70, 80, and 96% ethanol for 15 min each at RT. Subsequently, cells were immersed three times in 100% ethanol for 10 min. The slides with the cells were critical point dried with a CPD 300 (Leica Microsystems, Vienna, Austria) and sputter coated with 10 nm of gold with a sputter coater (Balzers Union, Liechtenstein). Samples were then examined with a scanning electron microscope using a magnification size of 5′000 and 50′000 (Zeiss EVO 40, Carl Zeiss Ltd, Cambridge, UK).

Transmission electron microscopy

One day prior to the experiments, BEAS-2B cells were trypsinized, seeded at 200′000 cells in 6-well plate in DMEM supplemented with 5% FCS, and allowed to adhere overnight at 37°C. The following day, cells were washed three times with DMEM supplemented with 17 mM HEPES and pretreated with inhibitors for 30 min at 37 °C at the indicated experiments. MBP-$1_{18\text{-}45}$ was preincubated with or without DNA and heparin for 15 min before addition to the cells for the indicated times at RT. At the end of the incubation time, cells were fixed in 2.5% glutaraldehyde in 0.15 M HEPES for at least 24 h before further processing.[80] Briefly, the samples were washed in a next step three times with 0.15 M HEPES, postfixed with 1% OsO_4 in 0.1 M Na-Cacodylate buffer for 1 h at 4°C, and washed again three times in 0.05 M maleic NaOH buffer. The samples were further dehydrated in 70%, 80%, and 96% ethanol for 15 min each at RT before immersion in 100% ethanol for three times for 10 min each, and finally in 1:1 ethanol-Epon overnight. The next day, cells were embedded in Epon and left to harden at 60°C for 5 days before cut to ultrathin sections. The sections were mounted on 200 mesh copper grids and stained with uranyless and lead citrate. Electron microscopy images were taken with a transmission electron microscope (Tecnai Spirit, Thermo Fisher Scientific) equipped with a digital camera (Veleta, Olympus, Soft Imaging System, Münster, Germany) and analyzed using FIJI software.

Liposome leakage assay

Total soy extract, total liver extract, cholesterol, and sphingomyelin mixed in a 4:4:1:1 ratio resulting in a final lipid mixture of approximately 35% phosphatidylcholine, 17% phosphatidylethanolamine, 16% phosphatidylinositol, 10% sphingomyelin, 10% cholesterol, 5% phosphatidylserine and 3% phosphatidic acid, or DOPC lipids were dissolved in chloroform. Chloroform was evaporated using an argon stream and the lipids were further dried overnight under vacuum. The following day, the lipid film was rehydrated in HBSS containing 50 mM 5(6)-carboxyfluorescein resulting in a total lipid concentration of 5 mg/mL and unilamellar vesicles were obtained by performing seven freeze-thaw cycles. The liposomes were sonicated on ice using a tip sonicator (Vibra Cell 75186, Thermo Fisher Scientific, Waltham USA) for 2 min with 30 s ON and 30 s OFF pulses and 40% amplitude. Outside dye was removed by gel filtration using a CentriPure MINI Desalt Z-50 column (emp BIOTECH GmbH, Berlin, Germany). MBP-$1_{18\text{-}45}$ was preincubated with or without heparin for 2 to 3 min and added to the liposomes (0.02 mg/mL) after 20 s of baseline measurement. Fluorescence intensity was measured using a PTI fluorescence spectrophotometer with an excitation wavelength of 490 nm, and an emission wavelength of 520 nm, and 10 nm slit width. Fluorescence was measured for 120 s before the addition of 0.1% Triton X-100 to assess maximum fluorescence. Fluorescence values were normalized to maximum fluorescence after subtraction of blank measurement.

Giant unilamellar vesicle (GUV)

GUV preparation

PVA GUV formation and microscopy slide preparation was performed using 2 mg/mL total soy extract, total liver extract, cholesterol, and sphingomyelin in a 4:4:1:1 ratio, resulting in a final lipid mixture of approximately 35% phosphatidylcholine, 17% phosphatidylethanolamine, 16% phosphatidylinositol, 10% sphingomyelin, 10% cholesterol, 5% phosphatidylserine and 3% phosphatidic acid, including 0.2 mol% DSPE-PEG2000-Biotin with addition of 1 mol% of Liss Rhod PE or Oregon 488 DHPE. HBSS containing 1 mM HPTS, 1 mM Calcein AM or 50 μM Dextran-TexasRed was used for lipid rehydration.

GUV imaging

Microscopy slides were imaged using an inverted fluorescence microscope (Nikon Ti-2 Eclipse with Crest X-light V2 spinning disk module (disk unit 60 μm), Nikon Europe BV, Amsterdam, Netherlands) with a CFI Plan Fluor 40× oil immersion objective (CFI Plan Fluor 40×/1.30 W.D. 0.24, Nikon Europe BV).[81] Brightfield and fluorescence images were recorded by an Andor Zyla 4.2 Plus USB3 camera in widefield and Spinning Disk Confocal mode using LED light excitation. HPTS/Calcein/Oregon 488 DHPE were imaged with excitation at 470 nm and emission at 515 nm using appropriate exciter, emitter, dichroic filter cubes. Liss Rhod PE was imaged with excitation at 550 nm and emission at 595 nm and TexasRed with excitation at 640 nm and emission at 698 nm using appropriate exciter, emitter, dichroic filter cubes. Time series were recorded with image acquisition every 10 s over 10 to 30 min.

Briefly, time series were started and after 30 s addition of final concentration of either 2.5 μM MBP-$1_{18\text{-}45}$, 2.5 μM MBP-$1^*_{18\text{-}45}$ or 1 μM alamethicin were performed. If present, final concentrations of 50 μM punicalagin were added before starting the time series. MBP-$1_{18\text{-}45}$ was preincubated with mtDNA or heparin before addition. Image analysis was performed using FIJI. GUVs were selected by hand and a background region of interest (ROI) was manually drawn for every GUV and subtracted from every GUV. Fluorescence

intensity was normalized to the average signal obtained for every GUV in the first 30 s of the time series. To visualize leakage, endpoint fluorescence of every GUV after a time series was depicted.

Cryo-electron microscopy

Total soy extract, total liver extract, cholesterol, and sphingomyelin, mixed in a 4:4:1:1 ratio, resulting in a final lipid mixture of approximately 35% phosphatidylcholine, 17% phosphatidylethanolamine, 16% phosphatidylinositol, 10% sphingomyelin, 10% cholesterol, 5% phosphatidylserine and 3% phosphatidic acid, were dissolved in chloroform. Chloroform was evaporated using an argon stream and the lipids were further dried overnight under vacuum. The following day, the lipid film was rehydrated in HBSS resulting in a total lipid concentration of 5 mg/mL and unilamellar vesicles were obtained by performing seven freeze-thaw cycles. The liposomes were sonicated on ice using a tip sonicator (Vibra Cell 75186, Thermo Fisher Scientific, Waltham USA) for 2 min with 30 s ON and 30 s OFF pulses and 40% amplitude.

For cyro-EM, 5 mg/mL liposomes were incubated with 1 μM MBP-$1_{18\text{-}45}$ for 20 min at RT before deposition onto a Lacey carbon grid that was glow discharged 10–20″ 10 mA using a Baltzers CTA 010. Next, the grids were plunged into liquid ethane in an atmosphere at 4°C and 100% humidity using a Vitrobot Mark IV. Vitrified grids were stored in liquid nitrogen before electron microscopy images were taken with a transmission electron microscope (Tecnai F20, FEI, Eindhoven, The Netherlands) equipped with a digital camera (Falcon III, Thermo Fisher Scientific) and analyzed using FIJI software.

Potassium concentration measurement

One day prior to the experiments, BEAS-2B cells were trypsinized, seeded at 50′000 cells in a 96-well plate in DMEM supplemented with 5% FCS and allowed to adhere overnight at 37°C. The following day, cells were washed three times with DMEM supplemented with 17 mM HEPES. MBP-$1_{18\text{-}45}$ was preincubated with or without DNA and heparin for 15 min at RT before addition to the cells for the indicated times. At the end of the incubation time, cells were collected by trypsinization and stained with 5 μg/mL IPG-1 AM for 20 min at 37°C. Potassium levels were assessed by flow cytometry (FACSVerse, BD Biosciences) and the MFI of the green channel was analyzed by FlowJo software (Tree Star, Ashland, OR, USA).

Calcium staining

One day prior to the experiments, BEAS-2B cells were trypsinized, seeded at 100′000 cells in a black glass-bottom 24-well plate in DMEM supplemented with 5% FCS, and allowed to adhere overnight at 37°C. The following day, cells were washed three times with DMEM supplemented with 17 mM HEPES and stained with 10 μM Fluo-3 AM and 1 μg/mL Hoechst 33342 for 30 min at 37°C before the cells were washed. Cells were treated with MBP-$1_{18\text{-}45}$ with or without DNA and analyzed in live cell microscopy experiments using confocal laser scanning microscopy (LSM 800, Carl Zeiss Micro Imaging GmbH, Jena, Germany) equipped with a Plan-Aprochromat 40x/1.4 Oil DIC objective. Ionomycin was used as a positive control. The images were subjected to analysis to measure MFI of Fluo-3 (green channel) using the automated surface module of Imaris software (Bitplane AG, Zurich, Switzerland).

QUANTIFICATION AND STATISTICAL ANALYSIS

GraphPad Prism 8 software (GraphPad Software Inc., La Jolla, CA, USA) was used for the analysis of all data. Data are expressed as the mean values ±SEM. Information about the n numbers and types of replicates, as well as about the statistical tests for each experiment are reported in the figure legends. To compare groups, one-way ANOVA with Tukey's multiple comparisons or two-way ANOVA with Dunnett's multiple comparisons test or Sidak's multiple comparisons was applied. p values ≤ 0.05 were considered statistically significant.